

An adaptive multiresolution flux reconstruction method with local time stepping and artificial viscosity for compressible flows simulations

Yixuan Lian, Jinsheng Cai, Shucheng Pan*

School of Aeronautics, Northwestern Polytechnical University, Xi'an, 710072, PR China

Abstract

In this paper, we introduce a novel approach that combines multiresolution (MR) techniques with the flux reconstruction (FR) method to accurately and efficiently simulate compressible flows. We achieve further enhancements in efficiency through the incorporation of local time stepping, and we add artificial viscosity to capture shocks. With the developed MR-FR algorithm, the layer difference of two adjacent elements can exceed 1, and simulation errors can be adjusted by manipulating a single scalar. To ensure conservation, information communication between nodes at different layers is accomplished using L^2 projection. Additionally, we propose an innovative indicator based on MR analysis to detect discontinuities, enabling us to take full advantage of the details generated by MR. By indicating smoothness and adding artificial viscosity only to the finest meshes, computational costs can be reduced and errors resulting from artificial diffusion can be locally limited. Numerical tests demonstrate that the adoption of MR preserve the convergence order of the FR method, and the newly proposed indicator performs well in detecting discontinuities. Overall, the MR-FR algorithm can accurately simulate compressible flows with strong shocks and physical dissipation using significantly fewer grids, making it a promising approach for further applications.

Keywords: Flux reconstruction, multiresolution, Local time stepping, Shock capturing, Artificial viscosity, Smooth indicator

1. Introduction

High-order methods in CFD are widely regarded as more effective than their low-order counterparts since they can achieve a given level of accuracy at a relatively lower computational cost [1]. In comparison to high-order methods in finite difference (FD) and finite volume (FV) schemes, those in finite element (FE) schemes can be adjusted for different orders more easily, mainly because their degrees of freedom (DoFs) lie in elements instead of stencils of points or cells. However, a higher number of DoFs leads to a considerable increase in computational cost, especially for a single layer of mass grids. To address the prohibitive cost of computation, the use of adaptive grids along with local time stepping can significantly reduce computational expenses.

*Corresponding author

Email address: shucheng.pan@nwpu.edu.cn (Shucheng Pan)

The flux reconstruction (FR) method was first proposed by Huynh in 2007 as an effective, robust, and simple method within the finite element scheme (FE) family [2]. In his pioneering work, Huynh thoroughly discussed the basic framework of flux reconstruction for solving 1D and 2D conservation laws, along with their corresponding stability, accuracy, and conservation. In 2009, Huynh expanded his work to include diffusion by reconstructing both solution and flux [3]. That same year, Wang and Gao proposed the lifting collocation penalty (LCP) method [4] for mixed meshes. Vincent et al. [5] later proposed a class of energy-stable FR schemes by varying a single scalar quantity, providing a new point of view on the stability of FR methods.

The utilization of the local grid adaptive technique enables dynamic refinement of meshes within the vicinity of intricate flow structures, such as shocks and vortexes. One of the primary challenges is determining how to trigger refining and coarsening. Some researchers have introduced sensors based on a gradient and/or rotation of certain flow variables, as reported in studies by Yang et al. [6–8]. Others have focused on using MR analysis to achieve the desired effect [9–13]. A representative example of sensor-based grid adaptation is J. Yang et al.’s work [6], where adaptive mesh refinement (AMR) is achieved within the framework of FR on moving/deforming mesh. In this work, the Mortar method, which is based on L^2 projection, is used to handle non-conforming interfaces, and artificial viscosity is added to capture shocks. Additionally, Yang proposed a unique data structure to address cells in this work. While different from AMR technique, MR method can provide better control of the error [12]. The core point of MR analysis is to represent data on the current level using data from a certain coarser level and differences, i.e., details, on successive refinement levels [14]. Gottschlich [15] initially introduced the concept of MR into FV to achieve grid adaptation. Shelton et al. [11] first combined the MR method with discontinuous Galerkin (DG) within FE family. Furthermore, Nils Gerhard developed a wavelet-free MR analysis and established a strategy to select threshold parameters for adaptive MR-DG schemes [12]. Wei Guo et al. further developed MR-DG in multiple dimensions, with adaptation realized according to the hierarchical surplus [16].

Discontinuous finite element schemes commonly employ limiters and artificial viscosity to mitigate or eliminate spurious oscillations caused by shocks in high-speed flows. Both techniques require flow detection, utilizing troubled-cell indicators for the former approach, and smoothness indicators for the latter. Exploiting that the details generated by multiwavelets decomposition suddenly increase around a discontinuity, Mathea et al proposed a global troubled-cell indicator based on multiwavelet [17]. This indicator, along with a minmod-type limiter, was later adopted by Nils Gerhard in an adaptive MR-DG scheme [12]. Similarly, Wei Guo et al. [16] suggested that hierarchical surplus can be used as a local smoothness indicator, enabling Juntao Huang et al. [13] to design an indicator guiding the addition of artificial viscosity in the adaptive MR-DG. In our work, we utilize artificial viscosity for shock capturing, and there are two types of artificial viscous stress: the physical type, which has a form consistent with Navier-Stokes viscous stress [6], and the Laplacian type [18], which is more simple in form and more robust in the presence of strong shocks [19].

The remainder of this article is organized as follows: In Sec. 2, we provide a brief overview of how to solve Navier-Stokes equations using FR method on a uniform grid. Sec. 3 describes the MR-FR algorithm, emphasizing the importance of information exchange between nodes at different levels, such as a parent and its children, and an

uncle and its nephews. In Sec. 4, we introduce artificial viscosity and smoothness indicators to capture shocks. Finally, in Sec. 5, we present several numerical examples to demonstrate the effectiveness of the proposed methods.

2. Flux reconstruction method on uniform grid

2.1. Governing equations

The 2D Navier-Stokes equations can be expressed in conservative form as

$$\frac{\partial \mathbf{U}}{\partial t} + \frac{\partial \mathbf{F}}{\partial x} + \frac{\partial \mathbf{G}}{\partial y} = 0, \quad (1)$$

where the conservative variable, x- and y-direction flux vectors are

$$\mathbf{U} = [\rho, \rho u, \rho v, E]^T, \quad (2)$$

and

$$\begin{aligned} \mathbf{F} &= \mathbf{F}_c + \mathbf{F}_v, \\ \mathbf{G} &= \mathbf{G}_c + \mathbf{G}_v, \end{aligned} \quad (3)$$

respectively. The convective flux vectors are

$$\mathbf{F}_c = \begin{Bmatrix} \rho u \\ p + \rho u^2 \\ \rho uv \\ u(E + p) \end{Bmatrix}, \quad \mathbf{G}_c = \begin{Bmatrix} \rho v \\ \rho uv \\ p + \rho v^2 \\ v(E + p) \end{Bmatrix}, \quad (4)$$

and the viscous flux vectors are

$$\mathbf{F}_v = - \begin{Bmatrix} 0 \\ \tau_{11} \\ \tau_{12} \\ u\tau_{11} + v\tau_{21} + k\partial T/\partial x \end{Bmatrix}, \quad \mathbf{G}_v = - \begin{Bmatrix} 0 \\ \tau_{11} \\ \tau_{12} \\ u\tau_{12} + v\tau_{22} + k\partial T/\partial y \end{Bmatrix}. \quad (5)$$

To fully characterize the system, we need to incorporate the equation of state, which is given by

$$p = \rho RT. \quad (6)$$

Additionally, the shear stress tensor in Eq. (5) is defined as

$$\tau_{ij} = \mu(u_{i,j} + u_{j,i}) + \lambda\delta_{ij}u_{k,k}, \quad i, j = 1, 2, \quad (7)$$

where μ is the dynamic viscosity coefficient, λ is the bulk viscosity coefficient, and they are related by Stokes' hypothesis, which states that $2\mu + 3\lambda = 0$. The Kronecker delta function, δ_{ij} , is also used as a notation. The shear stress tensor $u_{i,j}$ in Eq. (7) is given by

$$u_{i,j} = \frac{\partial u_i}{\partial x_j}, \quad i, j = 1, 2, \quad (8)$$

where u_i is the i -th component of velocity $\mathbf{V} = [u, v]^T$, and x_j is the j -th component of coordinate $\mathbf{x} = [x, y]^T$. The Fourier's thermal conducting term in Eq. (5) is expressed as

$$k \frac{\partial T}{\partial i} = \frac{\mu\gamma}{Pr} \frac{\partial e}{\partial i}, \quad i = x, y, \quad (9)$$

where γ is the specific heat ratio, and Pr is the Prandtl number. Additionally, the internal energy e is given by

$$e = \frac{E}{\rho} - \frac{u^2 + v^2}{2}. \quad (10)$$

2.2. Flux reconstruction formulation

The $(N+1)$ -order flux reconstruction (FR) method is utilized to solve the Navier-Stokes equation on a uniform grid. This method is characterized by reconstructed polynomials of N order. Our approach utilizes rectangular physical elements with dimensions of $\Delta x \times \Delta y$, coupled with square standard elements of dimension $[-1, 1] \times [-1, 1]$ as demonstrated in Fig. 1. The mapping between physical coordinates (x, y) and reference coordinates (ξ, η) is defined as

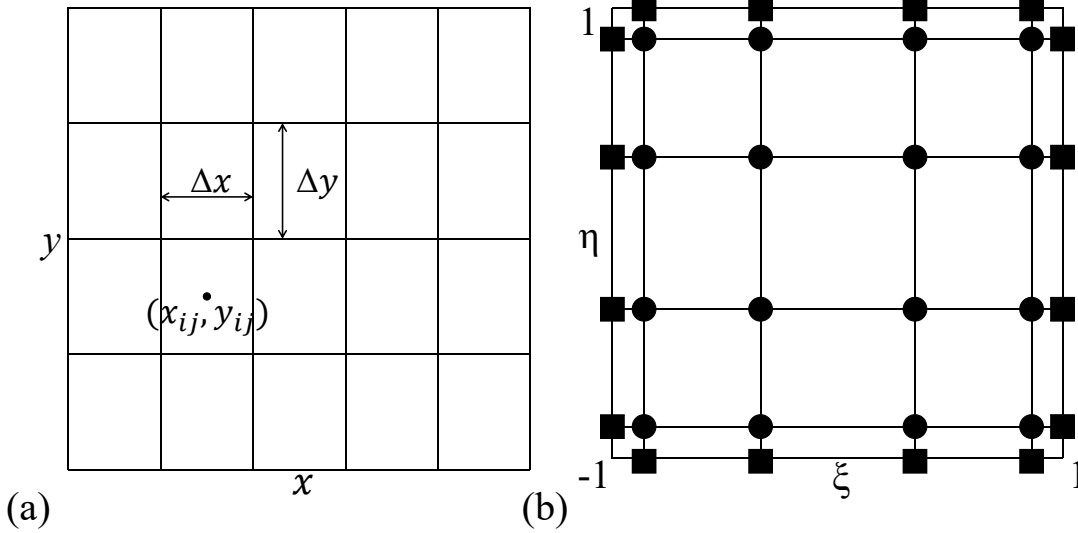


Figure 1: Physical grid element and standard computational element:(a) a block of uniform elements, and (b) distribution of SPs (circle) and FPs (square), $N = 3$

$$\begin{aligned} x(\xi) &= x_j + \xi \Delta x / 2, & \xi &\in [-1, 1], \\ y(\eta) &= y_j + \eta \Delta y / 2, & \eta &\in [-1, 1]. \end{aligned} \quad (11)$$

Here, (x_{ij}, y_{ij}) represents the center coordinate of the $(i$ -th, j -th) physical element. The standard element consists of $N_{\text{FP}} = 4(N + 1)$ flux points and $N_{\text{SP}} = (N + 1)^2$ solution points placed at Gauss-Legendre points, as illustrated in Fig. 1(b) for the case of $N = 3$. Transforming the governing equation, Eq. (1), through the coordinate transformation specified in Eq. (11), yields

$$\begin{aligned} \frac{\partial \hat{U}}{\partial t} + \frac{\partial \hat{F}}{\partial \xi} + \frac{\partial \hat{G}}{\partial \eta} &= 0, \\ \hat{U} &= \frac{\Delta x \Delta y}{4} \mathbf{U}, \\ \hat{F} &= \frac{\Delta y}{2} \mathbf{F}, \quad \hat{G} = \frac{\Delta x}{2} \mathbf{G}, \end{aligned} \quad (12)$$

where flux in ξ -direction and η -direction are denoted by \hat{F} and \hat{G} , respectively. The variables \hat{u} , \hat{f} , and \hat{g} are used to represent a specific component of \hat{U} , \hat{F} , and \hat{G} , respectively. Eq. (12) is then expressed as

$$\frac{\partial \hat{u}}{\partial t} + \frac{\partial \hat{f}}{\partial \xi} + \frac{\partial \hat{g}}{\partial \eta} = 0. \quad (13)$$

In the standard element, the reconstructed polynomial for \hat{u} with $\eta = \eta_s$ takes the form of

$$\hat{u}_i^C(\xi) = \hat{u}_i(\xi) + [\hat{u}_{i-1/2}^{\text{com}} - \hat{u}_i(-1)] g_{\text{LB}}(\xi) + [\hat{u}_{i+1/2}^{\text{com}} - \hat{u}_i(1)] g_{\text{RB}}(\xi). \quad (14)$$

Here, the superscript C represents continuity, and $\hat{u}_{i-1/2}^{\text{com}} / \hat{u}_{i+1/2}^{\text{com}}$ denote the common solutions located at the s -th flux point of the (i -th, j -th) element's left/right boundary. The correction functions, g_{LB} and g_{RB} [2], take the form of

$$\begin{aligned} g_{\text{LB}} &= R_{R,N+1} = \frac{(-1)^{(N+1)}}{2} (P_{N+1} - P_N), \\ g_{\text{RB}} &= R_{L,N+1} = \frac{1}{2} (P_{N+1} + P_N), \end{aligned} \quad (15)$$

where $R_{R,N+1}/R_{L,N+1}$ denote the $(N+1)$ -order right/left Radau polynomials, and P_N denotes a Legendre polynomial of order P . The uncorrected polynomial $\hat{u}_i(\xi)$ can be expressed as

$$\hat{u}_i(\xi) = \sum_{n=0}^N L_n(\xi) \hat{u}_{i,n}, \quad (16)$$

where u represents the nodal value at the (n -th, s -th) solution point and $L_n(\xi)$ is the Lagrange basis function (as shown in Eq. (A.25)). After taking the derivative of Eq. (14), we obtain

$$(\hat{u}_i^C)_\xi = (\hat{u}_i)_\xi + [\hat{u}_{i-1/2}^{\text{com}} - \hat{u}_i(-1)] g'_{\text{LB}} + [\hat{u}_{i+1/2}^{\text{com}} - \hat{u}_i(1)] g'_{\text{RB}} \quad (17)$$

where the independent variable ξ is dropped without ambiguity, and the superscript $'$ and the subscript ξ denote derivation. Moreover, for $\xi = \xi_t$, $(\hat{u}_j^C)_\eta$ can be acquired by

$$(\hat{u}_j^C)_\eta = (\hat{u}_j)_\eta + [\hat{u}_{j-1/2}^{\text{com}} - \hat{u}_j(-1)] g'_{\text{LB}} + [\hat{u}_{j+1/2}^{\text{com}} - \hat{u}_j(1)] g'_{\text{RB}}, \quad (18)$$

$$\hat{u}_j(\eta) = \sum_{m=0}^N L_m(\eta) \hat{u}_{j,m}, \quad (19)$$

where $\hat{u}_{j-1/2}^{\text{com}}/\hat{u}_{j+1/2}^{\text{com}}$ denotes the common solution at the t -th flux point of the (i -th, j -th) element's bottom/top boundary, and $\hat{u}_{j,m}$ stands for the nodal value at the (t -th, m -th) solution point. By replacing \hat{u} with \hat{f} in Eq. (17) and Eq. (16), the derivation of \hat{f} with respect to ξ can be obtained,

$$(\hat{f}_i^C)_\xi = (\hat{f}_i)_\xi + [\hat{f}_{i-1/2}^{\text{com}} - \hat{f}_i(-1)] g'_{\text{LB}} + [\hat{f}_{i+1/2}^{\text{com}} - \hat{f}_i(1)] g'_{\text{RB}}, \quad (20)$$

$$\hat{f}_i(\xi) = \sum_{n=0}^N L_n(\xi) \hat{f}_{i,n}. \quad (21)$$

Similarly, we get

$$(\hat{g}_j^C)_\eta = (\hat{g}_j)_\eta + [\hat{g}_{j-1/2}^{\text{com}} - \hat{g}_j(-1)] g'_{\text{LB}} + [\hat{g}_{j+1/2}^{\text{com}} - \hat{g}_j(1)] g'_{\text{RB}}. \quad (22)$$

$$\hat{g}_j(\eta) = \sum_{m=0}^N L_m(\eta) \hat{g}_{j,m}, \quad (23)$$

These formulas, namely Eq. (17) \sim Eq. (22), form the basis for the seven-stage algorithm of the flux reconstruction method for the Navier-Stokes equation [20].

- (i) Interpolate the nodal values of the solution using Eq. (16) and Eq. (19).
- (ii) Calculate \hat{u}^{com} using

$$\hat{u}^{\text{com}} = \kappa \hat{u}_L + (1 - \kappa) \hat{u}_R, \quad 0 \leq \kappa \leq 1, \quad (24)$$

where κ can be either 1/2 for average[21][22] or 0 (or 1) for bias[23]. The left and right values are obtained as $\hat{u}_L = \hat{u}_{j-1}(1)$ and $\hat{u}_R = \hat{u}_j(-1)$, respectively

- (iii) Evaluate the first derivative of the solution using Eq. (17) and Eq. (18).
- (iv) Calculate the inviscid and viscous fluxes at the solution point, and interpolate the nodal values of the flux using Eq. (21) and Eq. (23).
- (v) Calculate \hat{f}^{com} using a Riemann solver (e.g., Roe's flux or AUSM flux) for the inviscid part, and

$$\hat{f}^{\text{com}} = (1 - \kappa) \hat{f}_L + \kappa \hat{f}_R, \quad 0 \leq \kappa \leq 1; \quad (25)$$

for the viscous part.

- (vi) Acquire the continuous flux by correction and evaluate its derivative using Eq. (20) and Eq. (22);
- (vii) Time-march the following equation to obtain the solution,

$$\frac{\partial \hat{u}}{\partial t} = -\left(\frac{\partial \hat{f}}{\partial \xi} + \frac{\partial \hat{g}}{\partial \eta}\right). \quad (26)$$

2.3. Time marching scheme

For effective use of the local time stepping in MR technique outlined in Sec. 3.5, we employ the second-order accurate strong stability preserving (SSP) Runge-Kutta scheme [24],

$$\begin{aligned} \mathbf{U}^{(1)} &= \mathbf{U}^n + \Delta t \mathbf{R}(\mathbf{U}^n) \\ \mathbf{U}^{n+1} &= \frac{1}{2} \mathbf{U}^n + \frac{1}{2} \mathbf{U}^{(1)} + \frac{1}{2} \Delta t \mathbf{R}(\mathbf{U}^{(1)}). \end{aligned} \quad (27)$$

2.4. Positivity preservation scheme

In order to maintain the correct physical attributes of flow states during the time marching and data structure updating processes, it is essential that only positive density and pressure values are deemed admissible at any solution point or flux point. Unfortunately, negative values may still arise during these processes. To address this challenge, we utilize a positivity preservation algorithm that was originally developed for the DG scheme [25] [26] [27] and later extended to the FR scheme [28] [29]. Here, we present a brief summary of this algorithm to correct the unphysical states at flux points.

- (i) Compute the element-wise average state $\bar{\mathbf{u}}$,

$$\bar{\mathbf{u}} \stackrel{\text{def}}{=} \frac{1}{|\Omega|} \int_{\Omega} \mathbf{u} d\Omega, \quad (28)$$

and related density $\bar{\rho}$ and pressure $p(\bar{\mathbf{u}})$, and then define a small number,

$$\epsilon_1 \stackrel{\text{def}}{=} \min(10^{-13}, \bar{\rho}, p(\bar{\mathbf{u}})). \quad (29)$$

(ii) Limit the density at the i -th ($i = 1, 2, \dots, N_{\text{SP}}$) solution point to be positive by

$$\begin{aligned}\tilde{\rho}_i &= t_1 (\rho_i - \bar{\rho}) + \bar{\rho}, \\ t_1 &= \min \left(\frac{\bar{\rho} - \epsilon_1}{\bar{\rho} - \rho_{\min}}, 1 \right), \\ \rho_{\min} &= \min_{1 \leq j \leq N_{\text{FP}}} (\rho_j),\end{aligned}\tag{30}$$

where j is the index of flux point.

(iii) Refresh the states at the j -th ($j = 1, 2, \dots, N_{\text{FP}}$) flux point by extrapolating the density-limited states $\tilde{\mathbf{u}}_i = (\tilde{\rho}, \rho u, \rho v, E)$ at all solution points.

(iv) Solve the following second-order equation

$$p(t_j (\tilde{\mathbf{u}}_j - \bar{\mathbf{u}}) + \bar{\mathbf{u}}) = \epsilon_1, \quad 0 < t_j < 1\tag{31}$$

for each flux point with negative pressure, and finally we get the pressure-limited states at solution points by

$$\begin{aligned}\tilde{\tilde{\mathbf{u}}}_i &= t_2 (\tilde{\mathbf{u}}_i - \bar{\mathbf{u}}) + \bar{\mathbf{u}}, \quad i = 1, 2, \dots, N_{\text{SP}} \\ t_2 &= \min_{1 \leq j \leq n_j} (t_j),\end{aligned}\tag{32}$$

where n_j is the number of flux points with negative pressure.

The algorithm corrects unphysical states at solution points by solving Eq. (31) for each solution point with negative pressure and using ρ_{\min} (defined as the minimum density at all solution points in Eq. (30)).

3. FR method with multiresolution

To achieve an adaptive MR method, it is essential to have a dynamic data structure and a process for its adaptive updating. We describe each of these parts in detail in the following two subsections. Additionally, we illustrate the boundary conditions that are fulfilled by means of ghost elements for FR. Following this, we present the conservative flux computation for elements with non-conforming interfaces in the penultimate subsection. Finally, we provide an overview of the scale-dependent local time stepping method designed for adaptive MR in the last subsection [30].

3.1. Tree-type data structure

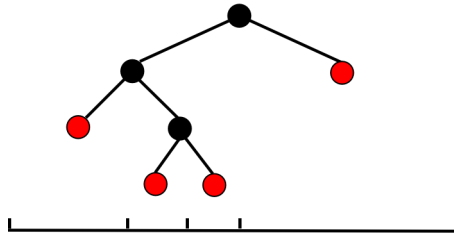


Figure 2: Tree-type data structure in 1D

Fig. 2 displays the tree-type data structure in 1D. Our data structure includes nodes that are siblings, cousins, and nephews, depending on their relationship with other nodes in the tree. Leaf nodes, indicated by red dots in Fig. 2, are nodes without any children. Each node contains just as many elements, whether it is a leaf or not.

3.2. MR analysis based on integral projection

To dynamically adapt the tree-type data structure, we perform MR analysis. In this process, we use integral projection [31] to handle bidirectional communication between a parent element and its children. Fig. 3 shows this communication in 2D. For the standard

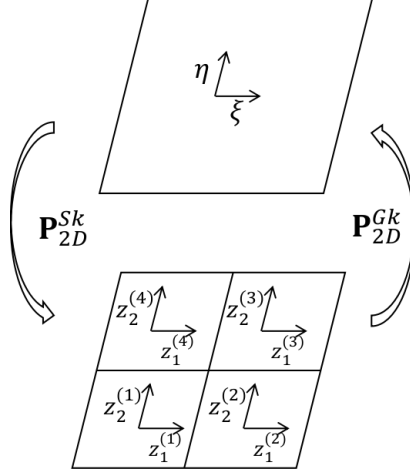


Figure 3: Projection between parent and children elements

elements, the coordinates (ξ, η) and the separate coordinates $(z_1^{(k)}, z_2^{(k)})$, corresponding to the parent element and four children elements, respectively, are related by

$$\begin{aligned} \xi &= s \cdot z_1^{(k)} + o_1^{(k)}, \eta = s \cdot z_2^{(k)} + o_2^{(k)}, \\ (\xi, \eta) &\in [-1, 1]^2, (z_1^{(k)}, z_2^{(k)}) \in [-1, 1]^2 \\ k &= 1, 2, 3, 4, \end{aligned} \quad (33)$$

where the scale parameter $s = 0.5$ and offsets $o_j^{(k)} = \pm 0.5$ depending on the index of children elements, k .

The scatter projection, as its name implies, scatters the information of a parent to its children. In 2D, the corresponding operation in matrix form is

$$\begin{aligned} q_i^{Ck} &= (\mathbf{P}_{2D}^{Sk})_{ij} q_j^P, \\ k &= 1, \dots, 4, \quad i, j = 0, \dots, N \end{aligned} \quad (34)$$

where q_i^{Ck} and q_j^P are nodal values of a child and its parent, respectively. The scatter matrix, \mathbf{P}_{2D}^{Sk} , is expressed as

$$\mathbf{P}_{2D}^{Sk} = \mathbf{V} \mathbf{M}^{-1} \mathbf{S}^{(k)} \mathbf{V}^{-1}, \quad (35)$$

where the matrices in the right-hand side are

$$\mathbf{V}_{ij} = \psi_j(\mathbf{r}_i), \quad (36)$$

$$\mathbf{M}_{ij} = \int_{-1}^1 \int_{-1}^1 \psi_j(z_1, z_2) \psi_i(z_1, z_2) dz_1 dz_2, \quad (37)$$

and

$$\mathbf{S}_{ij}^{(k)} = \int_{-1}^1 \int_{-1}^1 \psi_j(s \cdot z_1 + o_1^{(k)}, s \cdot z_2 + o_2^{(k)}) \psi_i(z_1, z_2) dz_1 dz_2, \quad (38)$$

respectively. ψ_j and \mathbf{r}_i in Eq. (36) are the basis functions and the coordinates of solution points in the standard element, respectively. The Vandermonde matrix, \mathbf{V} in Eq. (36), relates nodal values q_i and modal values \tilde{q}_j by

$$q_i = \mathbf{V}_{ij}\tilde{q}_j. \quad (39)$$

Letting ψ_i be Legendre polynomials, the Mass matrix, \mathbf{M} in Eq. (37), can be simplified as

$$\mathbf{M}_{ij} = \begin{cases} 0 & \text{if } i \neq j \\ \frac{2}{2i+1} \cdot \frac{2}{2j+1} & \text{if } i = j \end{cases}. \quad (40)$$

As for the integrals in Eq.(38), they are calculated via Gauss-Legendre quadrature formula

$$I(f) = \int_{-1}^1 \int_{-1}^1 f(x, y) d\sigma \approx \sum_{k=1}^n A_k f(x_k, y_k), \quad (41)$$

where n is the number of Gauss points, x_k and A_k are coordinates of Gauss points and corresponding quadrature weights, respectively. In fact, the scatter projection can be simplified into interpolation operation, which is proofed in Sec. A.1,

Reversely, the gather projection in 2D is carried out via

$$\begin{aligned} \mathbf{P}_{2D}^{Gk} &= s^2 \cdot \mathbf{V}\mathbf{M}^{-1}\mathbf{S}^{(k)T}\mathbf{V}^{-1}, \\ q_i^P &= \sum_{k=1}^4 (\mathbf{P}_{2D}^{Gk})_{ij} q_j^{Ck} \end{aligned} \quad (42)$$

where $\mathbf{S}^{(k)T}$ is the transpose of $\mathbf{S}^{(k)}$. In Sec. A.2, the gather projection is reviewed from the point of least square approximation of a given function. As shown in Fig. 4, there

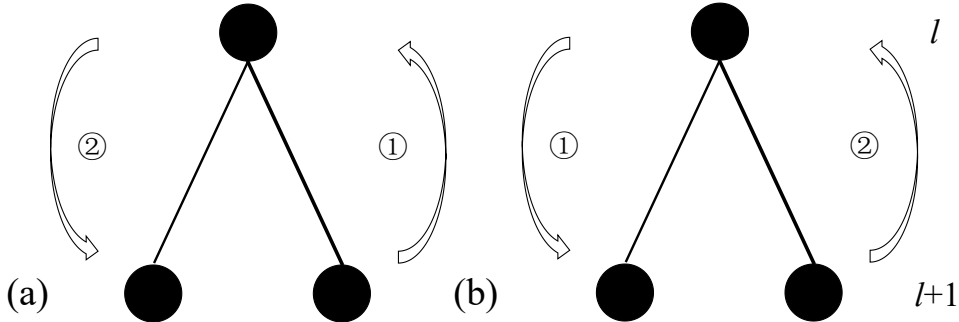


Figure 4: A pair of projection operators in two orders (in case of 1D): (a) ①Gather→②Scatter, and (b) ①Scatter→②Gather

are two different orders for a pair of projection operators in two adjacent levels. MR analysis follows Fig. 4(a) while Fig. 4(b) stands by the proof of outflow condition in Sec. A.3. MR analysis follows

- (i) Gather projection (Projection step in Ref. [10])

$$\bar{q}_i^P = \sum_{k=1}^4 (\mathbf{P}_{2D}^{Gk})_{ij} \bar{q}_j^{Ck}. \quad (43)$$

(ii) Scatter projection (Prediction step in Ref. [10])

$$\hat{q}_j^{Ck} = (\mathbf{P}_{2D}^{Sk})_{ji} \bar{q}_i^P, k = 1, \dots, 4. \quad (44)$$

(iii) Errors calculation for the j -th solution point of the k -th child

$$\hat{d}_j \stackrel{def}{=} \bar{q}_j^C - \hat{q}_j^C, \quad (45)$$

where k is dropped with no ambiguity.

The absolute errors calculated by Eq. (45) are called details [10] and furthermore, we define relative errors as

$$\hat{d}_j^r \stackrel{def}{=} \hat{d}_j / \bar{q}_j^C, \quad (46)$$

which can serve as smoothness indicators for the flow field (see Sec. A.4).

A leaf in a tree needs refining, if $\exists e, j$ s.t.

$$\left| \hat{d}_{e,j}^r \right| > \epsilon_l, \quad (47)$$

where e is the index of elements of this leaf. The level-dependent threshold ϵ_l is given as

$$\epsilon_l = 2^{D_0(l-L_{\max})} \epsilon, \quad (48)$$

where D_0 is the space dimension, and L_{\max} is the maximum level of adaptive data structure [32]. Once a leaf is refined, the scatter projection is carried out to initialize its newborn children.

As for coarseness, all children of a parent can be deleted simultaneously, only if they are all leaves and each of them satisfies that $\forall e, j$ s.t.

$$\left| \bar{d}_{e,j} \right| \leq \epsilon_l. \quad (49)$$

Obviously, the gather projection should be completed before children are deleted.

3.3. Boundary reconstruction

In the FR method, flux points have a crucial role in the boundary reconstruction process. Firstly, physical boundary conditions such as periodic and symmetry boundary conditions are applied by assigning certain states to flux points. Secondly, non-conforming interfaces, resulting from MR, are addressed through the Mortar method [33, 34], which involves bidirectional exchange of states and fluxes at flux points between real and auxiliary mortar elements. To apply physical boundary conditions and handle non-conforming interfaces, we introduce the concept of ghost elements, inspired by the two-step exchange method in Ref. [9]. Similar to the treatment of ghost cells in the finite volume method, we assign certain states to solution points of ghost elements to apply physical boundary conditions. A detailed description of the treatment for non-conforming interfaces follows.

As illustrated in Fig. 5, Node A and B, located at Level l , are neighbors, with Node A having four children, denoted as a_1, a_2, a_3, a_4 . Of the three leaf nodes in the tree, which are Node a_2, a_4 and B, two of them have non-conforming interfaces. The boundary reconstruction is carried out level by level. When reconstructing the boundaries for nodes at Level l , the states at all solution points of real Element B.1 are copied to ghost Element A.1, while the data of real Element A.2 is transferred to ghost Element B.2

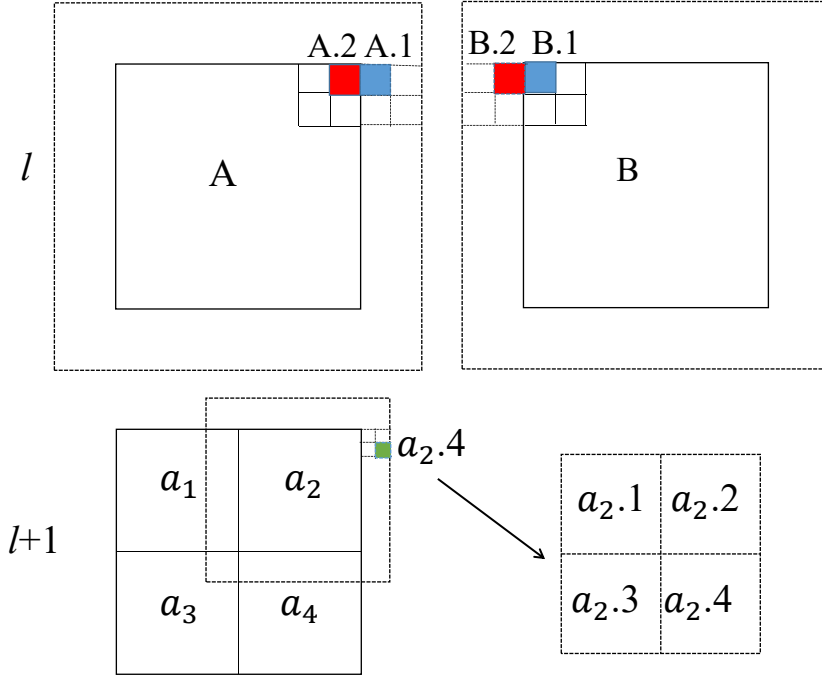


Figure 5: Boundary reconstruction for a node with non-conforming interfaces

using the same method. Subsequently, when we move on to the nodes at Level $l + 1$, the states of ghost Elements $a_{2.1}$ to $a_{2.4}$ are settled by scattering the states of ghost Element A.1. Thus, the non-conforming interface between Node a_2 and B is managed by Node A acting as the third party. Information flows as $B.1 \rightarrow A.1 \rightarrow a_{2.1} \sim a_{2.4}$. According to the seven-stage algorithm of FR method discussed in Sec. 2.2, we need two-layer ghost elements to solve viscous problems, as sketched in Fig. 5, while one-layer ghost elements are enough for inviscid problems.

3.4. Conservative flux computation

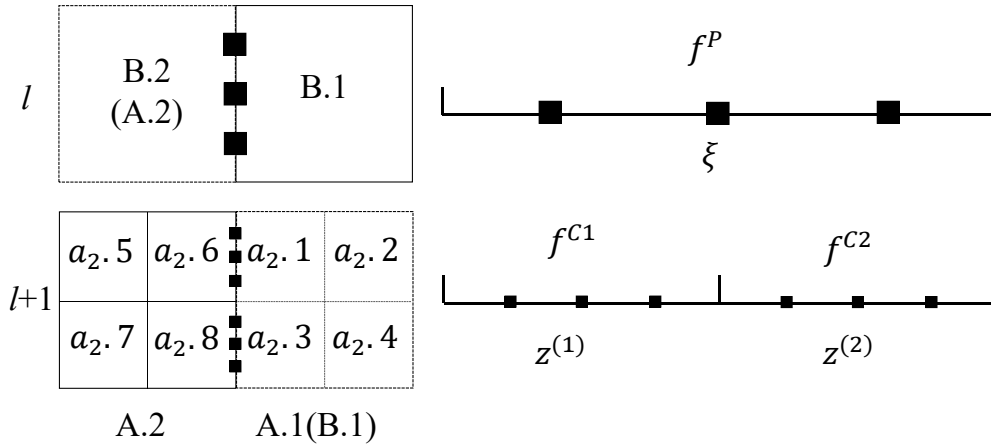


Figure 6: Conservative flux computation for a node with non-conforming interfaces

In order to alleviate the inconvenience of symbols, we substitute the common fluxes $\hat{f}_{i-1/2}^{\text{com}}$ and $\hat{g}_{j-1/2}^{\text{com}}$ in Sec.2.2 with just f in this subsection, which is unambiguous. By probing at the real and ghost elements in Fig. 5, Fig. 6 exhibits the fluxes of three real

elements, specifically B.1, $a_{2.6}$ and $a_{2.8}$, that share two non-conforming interfaces. We employ f^P to evolve the states of Element B.1 at Level l , whereas the fluxes f^{C1} and f^{C2} are utilized to evolve the states of Element $a_{2.6}$ and $a_{2.8}$, respectively, at Level $l+1$. Generally speaking,

$$\int_{-1}^1 f^P(\xi) d\xi \neq \sum_{k=1}^2 \int_{-1}^1 f^{Ck}(z^{(k)}) dz^{(k)}, \quad (50)$$

which spoils the conservation of flux. To preserve the conservation, we gather f^{C1} and f^{C2} via the 1D version of gather matrix (see Appendix A.2), i.e.,

$$\bar{f}_i^P \stackrel{def}{=} \sum_{k=1}^2 (\mathbf{P}_{1D}^{Gk})_{ij} f_j^{Ck} \quad i = 0, 1, \dots, N \quad (51)$$

where the subscripts i and j indicate the nodal form. According to the local conservation of gather projection, Eq. (A.38), we guarantee the flux conservation,

$$\int_{-1}^1 \bar{f}^P(\xi) d\xi = \sum_{k=1}^2 \int_{-1}^1 f^{Ck}(z^{(k)}) dz^{(k)}. \quad (52)$$

For better parallel performance, f^P is still used for evolving the states of Element B.1, while the increments of states caused by

$$\delta f^P \stackrel{def}{=} \bar{f}^P - f^P \quad (53)$$

are added to Element B.1 after every Runge-Kutta step.

3.5. Local time stepping

In adaptive grid methods, a large maximum refinement level L_{\max} can significantly limit the time step due to stability, resulting in decreased efficiency. To address this issue, X. Zhang et al.[8] introduced the continuous explicit Runge-Kutta method[35] to the work of Jingjing Yang [6] and achieving local time stepping in their AMR-FR. However, Wei Guo et al. identified that local time stepping was nontrivial to develop in their adaptive MR-DG scheme due to the distinct hierarchical basis functions employed. [16]. To overcome this limitation, we were motivated by the implementation of local time stepping in FV [30] and have applied this technique in our work. The extension to FR is straightforward and Fig. 7 depicts the time marching of elements in three successive levels.

As depicted in Fig. 7, the time evolution of RK1 and time interpolation occur only in step (*.1) of the algorithm. On the other hand, the time evolution of RK2 only takes place in step (*.2). After the execution of time interpolation, the new-born crossings, along with the dashed arrowheads at the finest level, are situated at the same position on the time axis. The modification of states at Level l takes effect only once the time evolution of RK2 is finished both at Level l and Level $l+1$.

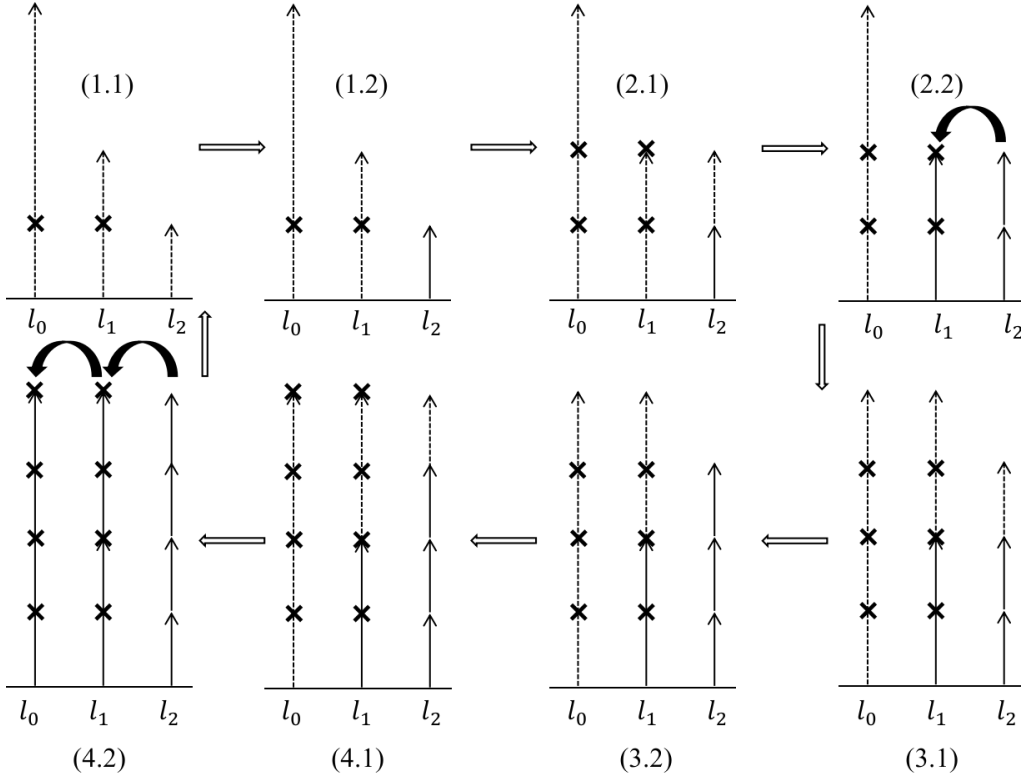


Figure 7: Local time stepping of multiresolution grid: $--\rightarrow$: time evolution of RK1 (the first substep of the second-order Runge-Kutta method); \rightarrow : time evolution of RK2; \times : time interpolation; \curvearrowright : modification of states to maintain flux conservation.

4. Shock capturing

4.1. Localized Laplacian artificial viscosity

As the name suggests, localized Laplacian artificial viscosity means that (i) the artificial dissipation is locally added around discontinuities, and (ii) the artificial viscosity, ε , is of Laplacian type[18], i.e.

$$\frac{\partial \mathbf{U}}{\partial t} + \nabla \cdot \mathbf{F} = \nabla \cdot (\varepsilon \nabla \mathbf{U}). \quad (54)$$

4.2. Smoothness indicator based on regularity analysis

To detect the discontinuity in flow fields and further add artificial dissipation precisely, smoothness indicator is needed, e.g.[18],

$$S_r = \frac{(q - q^{N-1}, q - q^{N-1})}{(q, q)} = \frac{\|q - q^{N-1}\|_2^2}{\|q\|_2^2}, \quad (55)$$

$$s_r = \log_{10} S_r$$

where q is the monitored variable such as density ρ or pressure p , and q^{N-1} is the unweighted L_2 projection of q on function space, \mathcal{P}_{N-1} (see Eq. (A.11)). The operator (\cdot, \cdot) is the standard inner product in \mathcal{L}_2 function space (see Eq. (A.31) and Eq. (A.12))[18] or the element-wise scalar product over the nodal values[29].

As mentioned in Sec.3.2 and discussed detailedly in Sec. A.4, the relative errors generated by regularity analysis can detect discontinuity. Specifically, we define the element-wise average of $|\hat{d}_j^r|$ as the smoothness indicator of the e -th element,

$$S_h \stackrel{def}{=} \frac{1}{|\Omega|} \int_{\Omega} |\hat{d}^r| d\Omega, \quad (56)$$

$$s_h = 2\log_{10}(S_h + \epsilon_2)$$

where Ω is the domain of the standard element, and ϵ_2 is introduced to avoid the base number to become 0, e.g. $\epsilon_2 = 10^{-7}$. Corresponding to the square of 2-Norm in Eq.(55), the factor multiplied by the logarithm in Eq. (56) is selected as 2. Since solution points are placed at Gauss-Legendre points, the integral above is evaluated via Eq.(41),

$$\int_{\Omega} |\hat{d}^r| d\Omega = \sum_{j=1}^{N_{SP}} A_j |\hat{d}_j^r|. \quad (57)$$

In contrast, Mathea et al. [17] utilized the absolute average of details to indicate troubled cells. Defining a norm of N_{SP} -dimensional real vector space $\mathbb{R}^{N_{SP}}$,

$$\|\mathbf{x}\|_{\omega} \stackrel{def}{=} \sum_{j=1}^{N_{SP}} |x_j| \omega_j, \quad (58)$$

$$\omega_j = A_j / |\Omega|,$$

$$\mathbf{x} = (x_1, \dots, x_{N_{SP}}) \in \mathbb{R}^{N_{SP}},$$

S_h in Eq. (56) is rewritten as

$$S_h = \left\| \hat{\mathbf{d}}^r \right\|_{\omega}, \hat{\mathbf{d}}^r = (\hat{d}_1^r, \dots, \hat{d}_{N_{SP}}^r) \in \mathbb{R}^{N_{SP}}. \quad (59)$$

In other word, S_h is the weighted L^1 -norm of vector $\hat{\mathbf{d}}^r$. Eq.(55) calculates the relative error between q and its projection in one order lower space, while Eq. (56) measures the relative error based on elements of two different sizes. Accordingly, we use subscript r and h respectively to indicate this difference.

4.3. Artificial viscosity coefficient

The element-wise artificial viscosity ε_e is calculated according to the smoothness indicator s_e [18]. This indicator uses subscript e to indicate element e instead of h in last subsection, without any ambiguity.

$$\varepsilon_e = \begin{cases} 0 & \text{if } s_e < s_0 - \kappa \\ \frac{\varepsilon_0}{2} \left(1 + \sin \frac{\pi(s_e - s_0)}{2\kappa} \right) & \text{if } s_0 - \kappa \leq s_e \leq s_0 + \kappa, \\ \varepsilon_0 & \text{if } s_e > s_0 + \kappa \end{cases}, \quad (60)$$

where the reference smoothness, s_0 , is suggested to be $-3\log_{10} N$, and the parameter κ , managing the working domain of artificial viscosity, plays a more important role than others [36]. The maximum of artificial viscosity, ε_0 , is evaluated as

$$\varepsilon_0 = \left(-\frac{\Delta\xi_{\max}}{Pe} + \frac{2}{Pe} \right) h|\lambda|_{\max}, \quad (61)$$

where the sub-cell resolution $\Delta\xi_{\max}$, is the maximum distance between two neighboring solution points in the standard element, h is the characteristic length of this element, $|\lambda|_{\max}$ is the maximum eigenvalue, and Pe is the Péclet number. It is worth noting that these parameters are problem-specific and require fine-tuning. To address this concern, Guido Lodato has proposed a self-calibration algorithm for the parameters s_0 and κ . The algorithm employs a relatively sharp hyperbolic tangent profile as a manufactured solution[19]. Bilateral interpolation of ε_V , the artificial viscosity at vertices, is conducted to achieve a smoother distribution of ε . Before this, ε_V has been calculated by averaging ε_e of elements around this vertex[36] [37].

Using the MR method described in the previous section, discontinuities are anticipated to be resolved in the finest grids, thus enabling the application of smoothness indication and artificial viscosity addition only at Level L_{\max} , resulting in reduced errors and computational cost [6, 12, 13].

5. Numerical examples

The paper provides numerical examples to validate and assess the accuracy of the methods and techniques discussed earlier. Specifically, for scenarios that exhibit discontinuity, artificial viscosity is applied solely to leaf nodes at Level L_{\max} to enhance the computation efficiency. The reference results are obtained through the FD method, using a 5-order WENO scheme for advection terms and a 4-order central difference scheme for diffusion terms, to provide a basis for comparison.

5.1. Euler vortex flow

In the first example, an Euler vortex flow is chosen to assess the order of the MR-FR method. This benchmark problem is based on the analytical solution presented in Ref. [6] that describes the flow field at time t .

$$\begin{aligned}
u &= U_\infty \left\{ \cos \theta - \frac{\epsilon_v y_r}{r_c} \exp \left(\frac{1 - x_r^2 - y_r^2}{2r_c^2} \right) \right\}, \\
v &= U_\infty \left\{ \sin \theta + \frac{\epsilon_v x_r}{r_c} \exp \left(\frac{1 - x_r^2 - y_r^2}{2r_c^2} \right) \right\}, \\
\rho &= \rho_\infty \left\{ 1 - \frac{(\gamma - 1)(\epsilon_v M_\infty)^2}{2} \exp \left(\frac{1 - x_r^2 - y_r^2}{r_c^2} \right) \right\}^{\frac{1}{\gamma-1}}, \\
p &= p_\infty \left\{ 1 - \frac{(\gamma - 1)(\epsilon_v M_\infty)^2}{2} \exp \left(\frac{1 - x_r^2 - y_r^2}{r_c^2} \right) \right\}^{\frac{\gamma}{\gamma-1}}, \\
x_r &= x - x_0 - (U_\infty \cos \theta)t, \quad y_r = y - y_0 - (U_\infty \sin \theta)t.
\end{aligned} \tag{62}$$

The parameters for mean flow are

$$\begin{aligned}
\theta &= \frac{\pi}{4}, \quad \gamma = 1.4, \\
U_\infty &= \sqrt{2} \text{ m/s}, \quad p_\infty = 1.0 \text{ Pa}, \quad \rho_\infty = 1.0 \text{ kg/m}^3, \\
c_\infty &= \sqrt{\frac{\gamma p_\infty}{\rho_\infty}} = \sqrt{1.4} \text{ m/s}, \\
M_\infty &= \frac{U_\infty}{c_\infty} = \sqrt{\frac{2}{1.4}} \approx 1.195,
\end{aligned}$$

where θ is the velocity direction of the mean flow, as well as the movement direction of the vortex. The parameters for the vortex are

$$r_c = 1.0 \text{ m}, \quad x_0 = y_0 = \frac{1}{2}L = 5\text{m},$$

$$\epsilon_v = \frac{5}{2\sqrt{2}\pi} \approx 0.56,$$

where (x_0, y_0) is the initial center of the vortex, L is the side length of the square computation domain, r_c and ϵ_v are the vortex size and strength, respectively. The initial conditions are established by setting $t = 0$ in Eq.(62) and periodicity is imposed along the four domain boundaries. Given these conditions, the analytical solution at time t is obtained through the substitution of x_r and y_r in Eq.(62) with

$$x_r = x_r - \left\lfloor \frac{x_r + x_0}{L} \right\rfloor \cdot L$$

$$y_r = y_r - \left\lfloor \frac{y_r + y_0}{L} \right\rfloor \cdot L$$
(63)

with $\lfloor \cdot \rfloor$ being the floor operator. Following Ref. [29], the L_1 - and the L_2 -norm of density are defined as

$$L_1(\epsilon_\rho) = \sum_{n=1}^{N_e} \int_{\Omega_n} |\epsilon_\rho| d\Omega_n \approx \sum_{n=1}^{N_e} J_n \sum_{j=1}^N |\epsilon_{\rho,j}| A_j$$

$$L_2(\epsilon_\rho) = \sqrt{\sum_{n=1}^{N_e} \int_{\Omega_n} \epsilon_\rho^2 d\Omega_n} \approx \sqrt{\sum_{n=1}^{N_e} J_n \sum_{j=1}^N \epsilon_{\rho,j}^2 A_j},$$

$$\epsilon_\rho = \rho - \rho_{exact}, \quad J_n = \Delta x_n \Delta y_n / 4$$
(64)

with N_e , J_n , Ω_n and A_j being the number of elements, the Jacobian determinant of the n -th element, the standard element of the n -th element and the j -th quadrature weight, respectively. The leaf node of the tree corresponds to a square block containing n_e^2 elements. Thus, we have $N_e = n_e^2 N_{leaf}$ and $J_n = (\Delta x_l)^2 / 4$, where N_{leaf} is the number of leaves in the tree, and Δx_l is the side length of the elements at level l . We set simulation parameters as follows: the threshold ϵ in Eq.(48) is 10^{-3} , and the number of solution points in each element N_{SP} is 4^2 . The tree has a maximum level of $L_{max} = 3$, corresponding to levels $l = 0, 1, 2, 3$. The total simulation time is $T_{total} = 10\text{s}$, and we vary the resolution by changing n_e among 2, 4, 8, and 16. The initial level of the tree is $l = 0$ with $N_0 = 1$ node. The periodic movement of the Euler vortex with $n_e = 8$ is illustrated in Fig. 8. Here, the blocks representing the vortex exactly align with the leaves at level L_{max} while other blocks are situated at coarser levels. The order of accuracy of FR-MR is displayed in Fig. 9. The characteristic spacing of the MR grid, denoted as Δx_{eff} , is computed as $L/\sqrt{N_e}$ [29]. Linear regression is then performed on the data points to determine the order of accuracy. The resulting slopes of the two straight lines fitted to these points denote the order of accuracy. Our numerical experiment confirms that the accuracy of FR-MR has been attained as expected.

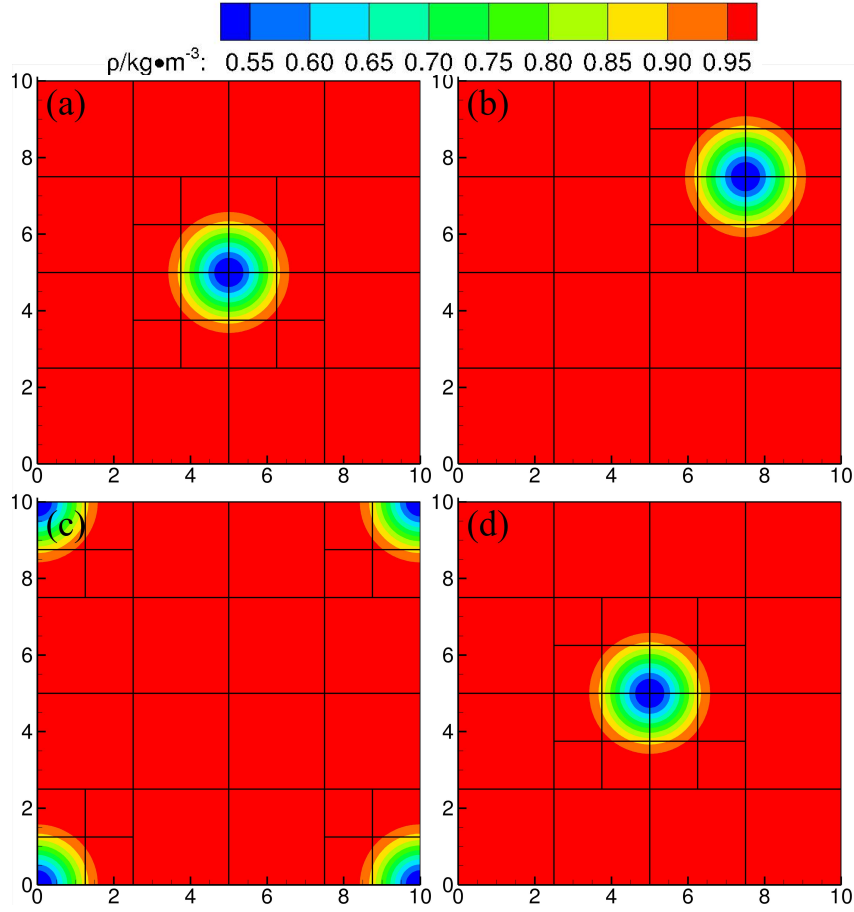


Figure 8: Density contours of the Euler vortex flow at four separate moments of a movement period: (a) $t=0.0\text{s}$, (b) $t=2.5\text{s}$, (c) $t=5.0\text{s}$ and (d) $t=10.0\text{s}$. Each block contains 8^2 elements.

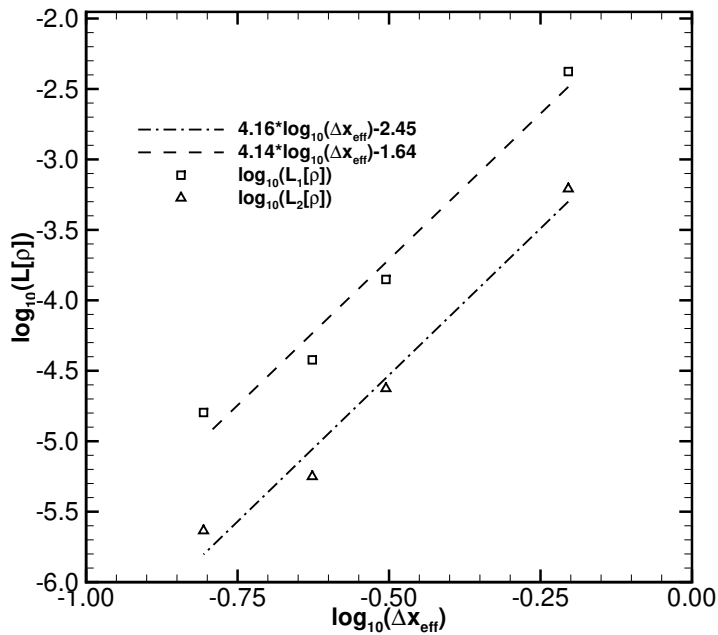


Figure 9: The convergence order of MR-FR: 4^2 solution points are placed in each element denoting a 4-order FR scheme, and each block contains n_e^2 ($n_e = 2, 4, 8, 16$) elements. The separate points are fitted by linear regression.

5.2. SOD's shock tube

The classical Sod's shock tube problem is elected to validate the shock capturing techniques present in Sec. 4. The initial condition is

$$\begin{cases} (\rho, u, p)_R = (0.125 \text{ kg/m}^3, 0 \text{ m/s}, 0.1 \text{ Pa}) & x > 0.5 \text{ m} \\ (\rho, u, p)_L = (1.0 \text{ kg/m}^3, 0 \text{ m/s}, 1.0 \text{ Pa}) & x \leq 0.5 \text{ m} \end{cases} \quad (65)$$

and the computation domain is $[0, 1.0\text{m}]$. Several parameters are used for the simulations,

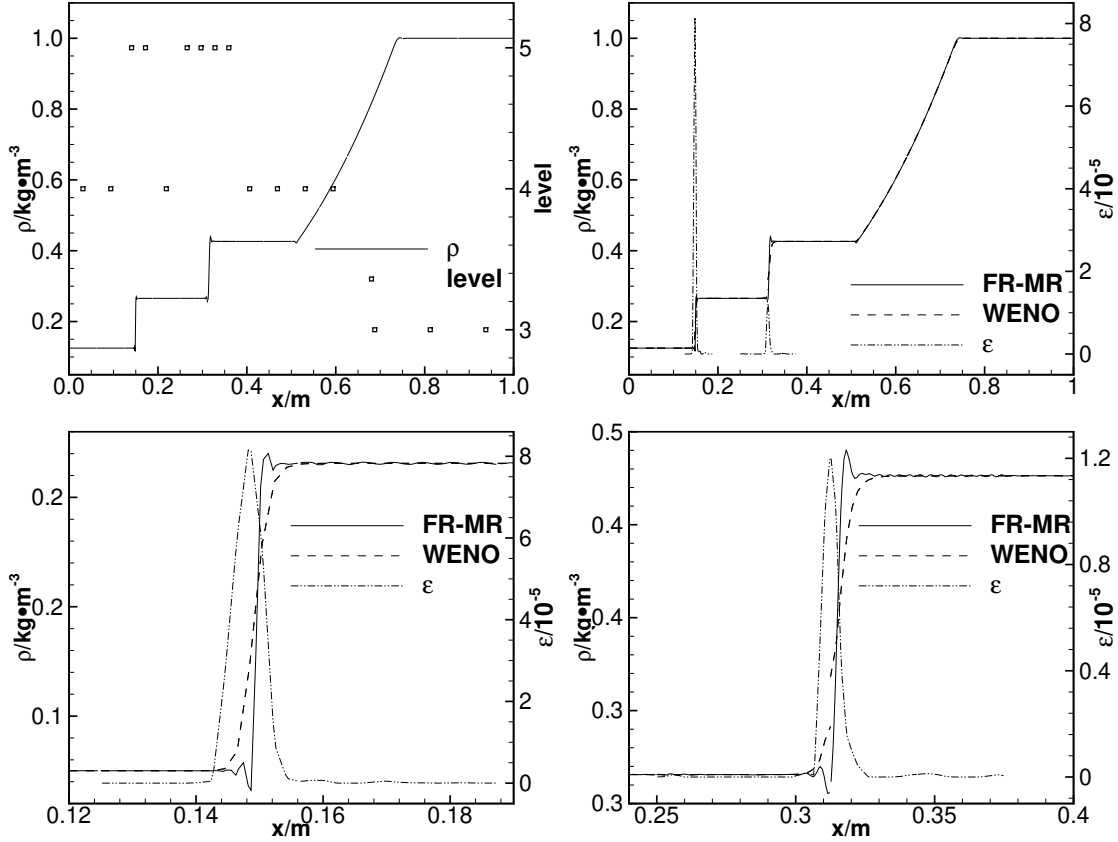


Figure 10: SOD's shock tube: (a) the density profile and the block-wise level distribution, (b) a global view of the distribution of artificial viscosity and the density profiles obtained by FR-MR and WENO, (c) the enlarged view of the shock, and (d) the enlarged view of the contact discontinuity. FR-MR: 3-order FR scheme on a MR grid with an effective resolution of 512; WENO: 5-order WENO scheme on a uniform grid with 512 cells.

namely $N_{\text{SP}} = 3$, $\epsilon = 0.01$, $L_{\text{max}} = 5$, $n_e = 16$, $N_0 = 1$, and $T_{\text{total}} = 0.2\text{s}$. The reference solution is obtained using FD with a classical 5-order WENO scheme on a grid with 512 uniformly spaced cells. Fig. 10(a) show that the MR algorithm successfully resolved both the shock and contact discontinuity at the finest grid resolution. Additionally, Fig. 10(b) presents the density profiles, which include the effects of artificial viscosity. By zooming in, Fig. 10(c) and Fig. 10(d) provide a more detailed view of the shock and contact discontinuity, respectively. It is evident from these figures that artificial viscosity is added only in the vicinity of discontinuities, leading to well-fitted density profiles despite some slight oscillations.

5.3. Shock-density wave interaction

In this subsection, the Shu-Osher problem [24] is considered, which simulates the interaction of a shock and an entropy wave. The initial condition is prescribed as

$$\begin{cases} (\rho_L, u_L, p_L) = (3.857143 \text{ kg/m}^3, 2.629369 \text{ m/s}, 10.3333 \text{ Pa}) & \text{if } x < 1 \text{ m,} \\ (\rho_R, u_R, p_R) = (1 + 0.2 \sin(5x) \text{ kg/m}^3, 0.0 \text{ m/s}, 1.0 \text{ Pa}) & \text{if } x \geq 1 \text{ m} \end{cases} \quad (66)$$

and the computation domain is $[0, 10\text{m}]$. Several parameters are considered for the sim-

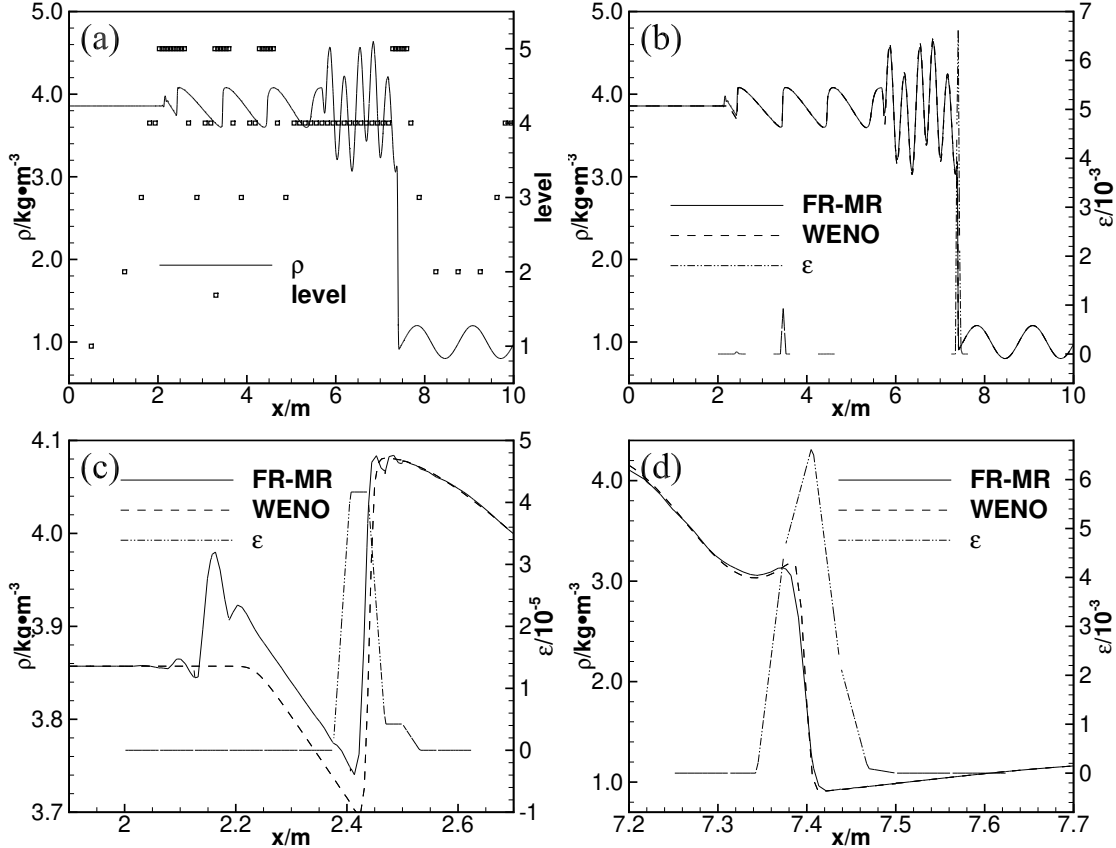


Figure 11: Shock-density wave interaction: (a) the density profile and the block-wise level distribution, (b) a global view of the distribution of artificial viscosity and the density profiles obtained by FR-MR and WENO, (c) the enlarged view of a weak discontinuity, and (d) the enlarged view of a strong discontinuity. FR-MR: 5-order FR scheme on a MR grid with an effective resolution of 320; WENO: 5-order WENO scheme on a uniform grid with 1600 cells.

ulation, which are as follows: $N_{\text{SP}} = 5$, $\epsilon = 0.01$, $L_{\text{max}} = 5$, $n_e = 2$, $N_0 = 5$, and $T_{\text{total}} = 1.8\text{s}$. Fig. 11 displays the simulation results along with the reference solution obtained on a uniform grid with 1600 cells. The employed MR algorithm automatically locates discontinuities at the finest grids, as evidenced by Fig. 11(a). Moreover, density profiles shown in Fig. 11(b) (d) agree well between results, particularly at $x = 7.4\text{m}$, where a strong discontinuity is clearly captured. However, minor oscillations are noticeable in the vicinity of $x = 2.4\text{m}$, where a weaker discontinuity is present. It is also noteworthy that artificial viscosity is locally and properly added.

5.4. 2D Kelvin-Helmholtz instability

In this subsection, the 2D Kelvin-Helmholtz instability problem is evaluated using the proposed MR-FR method. The box-shaped flow field with a size of $[0, D]^2$ is initialized

based on Ref. [38],

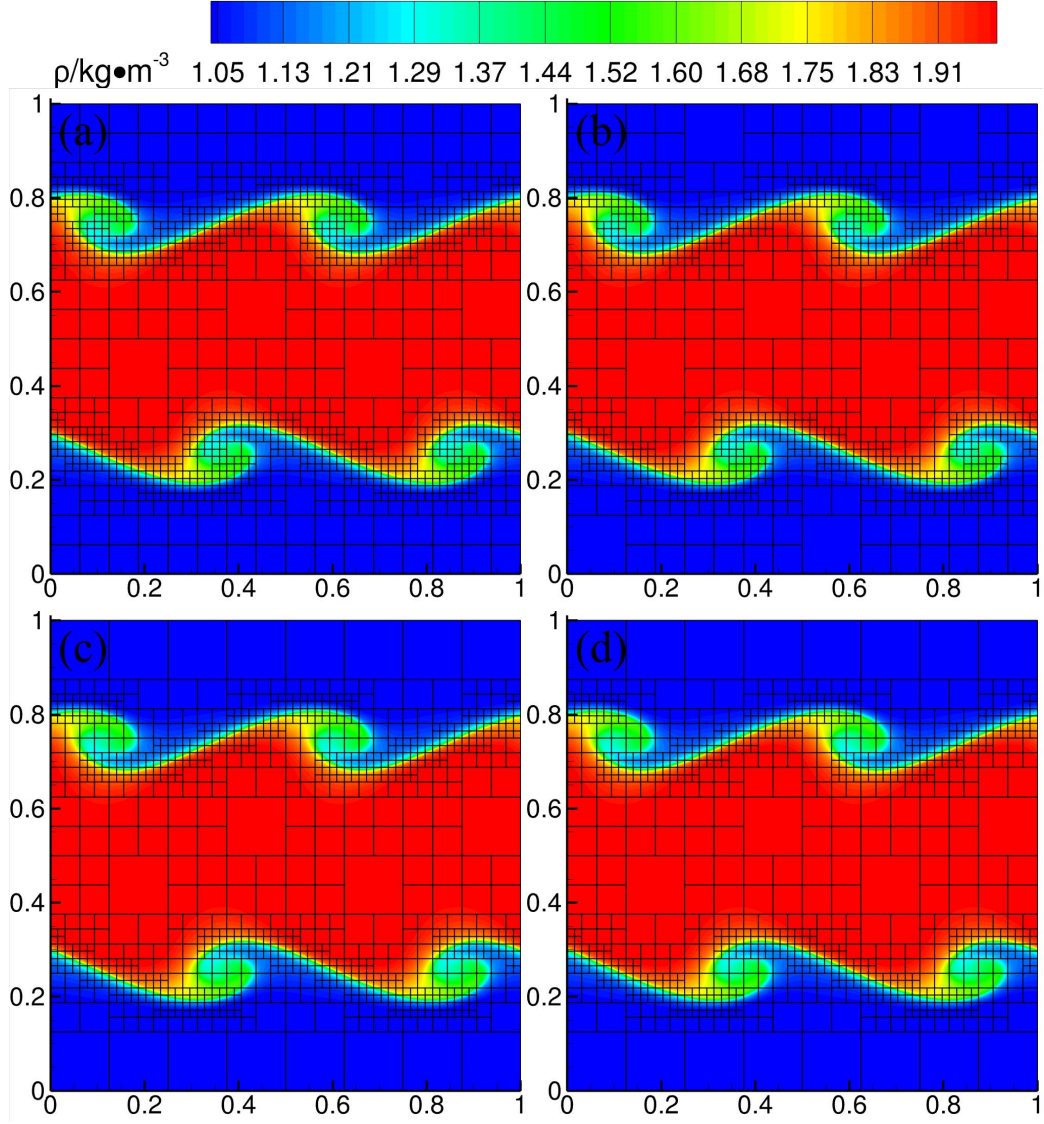


Figure 12: 2D Kelvin-Helmholtz instability: density contours at $t = 1.5s$ for four different orders (a) $N_{SP} = 3^2$, (b) $N_{SP} = 4^2$, (c) $N_{SP} = 5^2$, and (d) $N_{SP} = 6^2$.

$$\rho = \begin{cases} \rho_1 - \rho_m e^{\frac{-y/D+3/4}{L/D}}, & \text{if } 1 > y/D \geq 3/4 \\ \rho_2 + \rho_m e^{\frac{y/D-3/4}{L/D}}, & \text{if } 3/4 > y/D \geq 1/2 \\ \rho_2 + \rho_m e^{\frac{-y/D+1/4}{L/D}}, & \text{if } 1/2 > y/D \geq 1/4 \\ \rho_1 - \rho_m e^{\frac{y/D-1/4}{L/D}}, & \text{if } 1/4 > y/D \geq 0 \end{cases}$$

$$u = \begin{cases} u_1 - u_m e^{\frac{-y/D+3/4}{L/D}}, & \text{if } 1 > y/D \geq 3/4 \\ u_2 + u_m e^{\frac{y/D-3/4}{L/D}}, & \text{if } 3/4 > y/D \geq 1/2 \\ u_2 + u_m e^{\frac{-y/D+1/4}{L/D}}, & \text{if } 1/2 > y/D \geq 1/4 \\ u_1 - u_m e^{\frac{y/D-1/4}{L/D}}, & \text{if } 1/4 > y/D \geq 0 \end{cases} \quad (67)$$

where $\rho_m = (\rho_1 - \rho_2) / 2$ and $u_m = (u_1 - u_2) / 2$, and the y-direction velocity v is given by

$$\frac{v}{u_m} = \lambda \sin\left(\frac{\phi x}{D}\right). \quad (68)$$

The physical variables of the system are: $\rho_1 = 1.0, \rho_2 = 2.0, u_1 = 0.5, u_2 = -0.5, L = 0.025, D = 1.0, \lambda = 0.02$ and $\phi = 4\pi$. Additionally, the pressure is uniformly set to 2.5. The numerical simulation parameters include: $\epsilon = 0.01, L_{\max} = 6, n_e = 4, N_0 = 1$, and $T_{\text{total}} = 1.5\text{s}$. To achieve four different orders, solution points in each element are varied to $N_{\text{SP}} = 3^2, 4^2, 5^2$ and 6^2 . Due to the absence of discontinuities in the initial flow field, the use of shock capturing schemes is not necessary.

In Fig. 12, we observe the simulation results of four orders at $t = 1.5\text{s}$, which demonstrate good agreement with each other. The results validate the multiresolution method as billows of vortices are resolved at finer grids. However, the consistency of the distribution of blocks with different sizes is not identical across the four cases. This inconsistency can be attributed to various solution points and the shared threshold value used in the four cases.

5.5. 2D Rayleigh Taylor instability

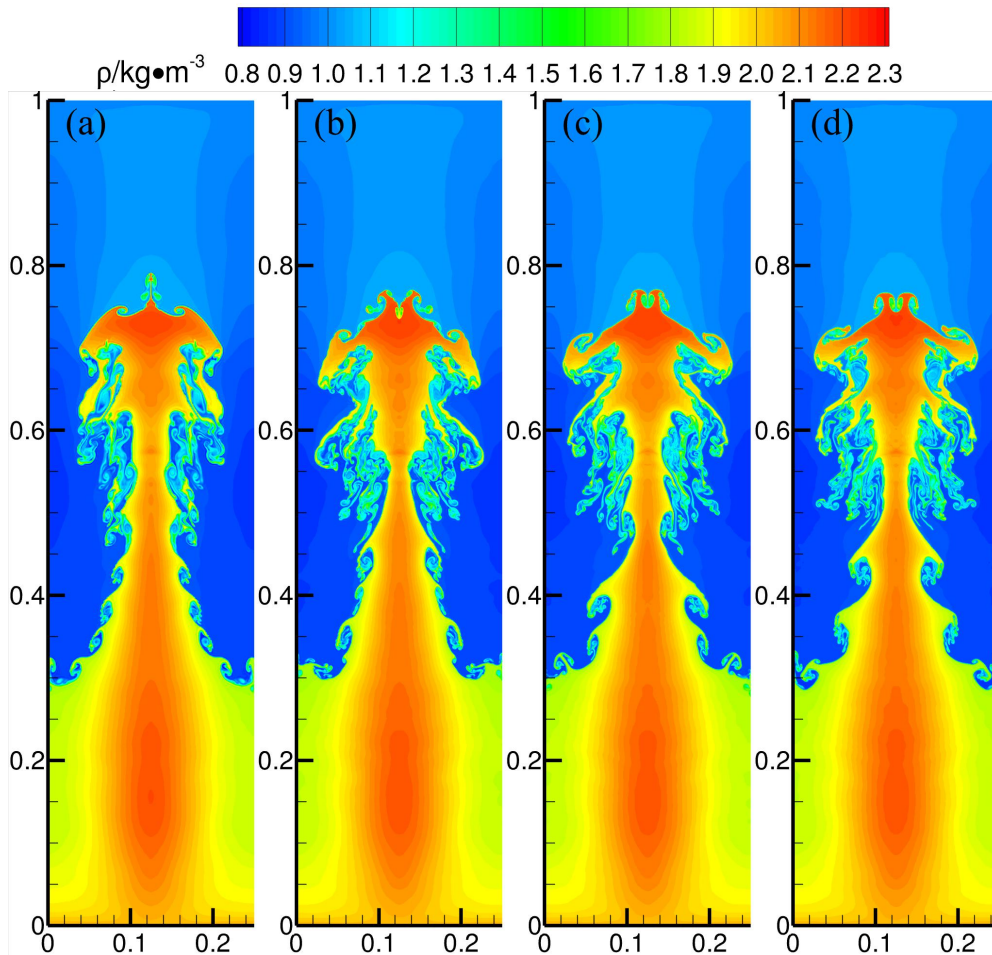


Figure 13: 2D Rayleigh Taylor instability: density contours at $t = 1.95\text{s}$ for four different orders (a) $N_{\text{SP}} = 3^2$, (b) $N_{\text{SP}} = 4^2$, (c) $N_{\text{SP}} = 5^2$, and (d) $N_{\text{SP}} = 6^2$.

To validate the ability of capturing contact discontinuity, we select a 2D Rayleigh Taylor instability problem. The initial conditions are prescribed as

$$\begin{cases} \rho = 2, u = 0, v = -0.025c \cdot \cos(8\pi x), p = 2y + 1, (y \leq 0.5) \\ \rho = 1, u = 0, v = -0.025c \cdot \cos(8\pi x), p = y + 1.5, (y > 0.5) \end{cases}, \quad (69)$$

where $c = \sqrt{\gamma P/\rho}$, with the computation domain set at $[0, 0.25m] \times [0, 1.0m]$. All physical variables used are in SI units. To introduce gravity, a source term, expressed as $S = (0, \rho, 0, \rho v)$ is added to the governing equation. Some numerical parameters utilized in this case include $\epsilon = 0.01$, $L_{\max} = 5$, $n_e = 4$, $N_0 = 1 \times 4$, and $T_{\text{total}} = 1.95s$. Four simulations are carried out with different orders, i.e., $N_{\text{SP}} = 3^2, 4^2, 5^2$ and 6^2 , just as we did in Sec. 5.4, while the difference is that artificial viscosity is needed in this problem.

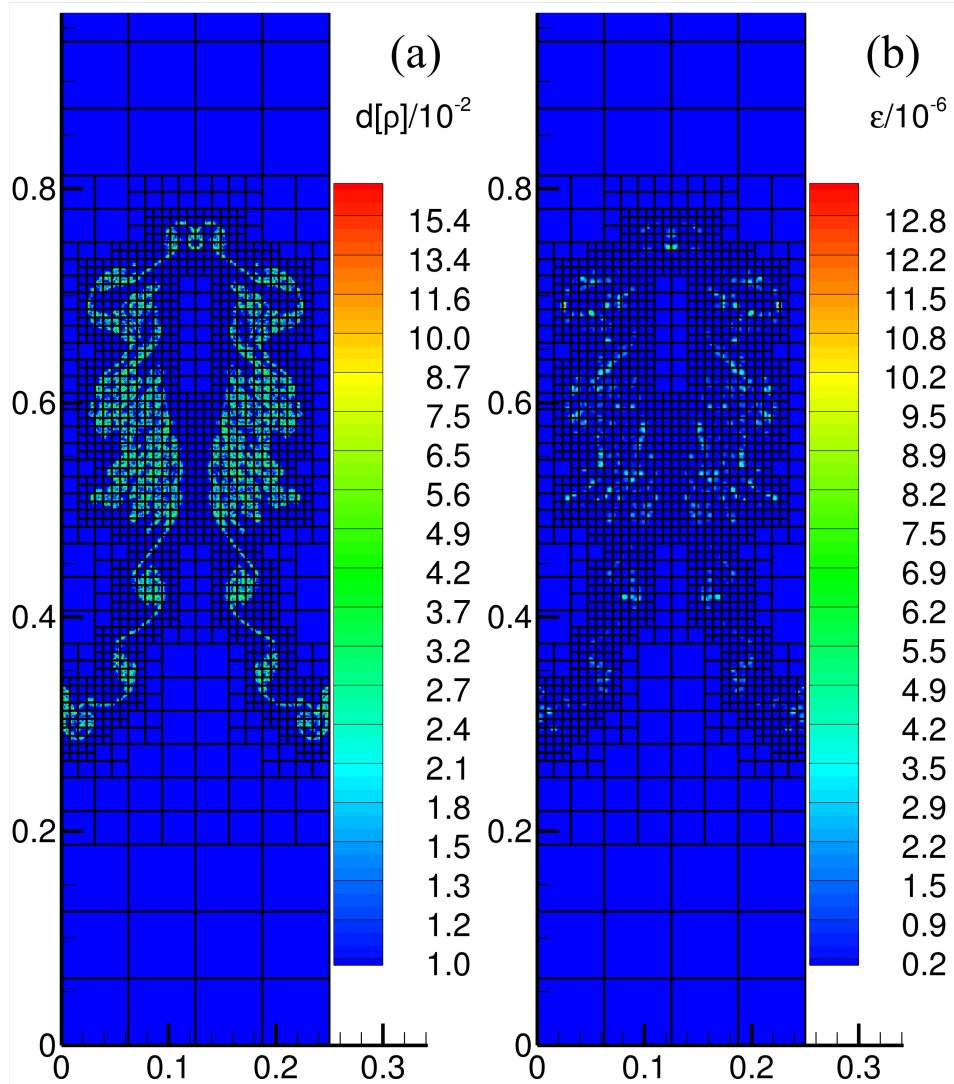


Figure 14: 2D Rayleigh Taylor instability for $N_{\text{SP}} = 6^2$: (a) details of density with exponentially distributed levels, and (b) the distribution of artificial viscosity.

Fig. 13 displays the density contours at $t = 1.95s$. In contrast to cases in Sec. 5.4, the four density contours exhibit differences because of the absence of grid convergence for this specific problem. Taking $N_{\text{SP}} = 6^2$ for an example, we display the details of

density and artificial viscosity in Fig. 14. The details of density accurately identify contact discontinuities, allowing artificial viscosity to be added to these regions. However, due to the smoothness indicator cut-off in Eq.(60), the artificial viscosity distribution is less continuous than the details of density.

5.6. 2D Riemann problem

To evaluate the effectiveness of the proposed method in capturing shocks in two dimensions, we first consider a 2D Riemann problem. We select the interaction of two shocks as the test case, with initial conditions specified as [38]

$$(\rho, u, v, p)(x, y, 0) \begin{cases} (1.5, 0, 0, 1.5), & x > 0.5, y > 0.5, \\ (0.5323, 1.206, 0, 0.3), & x < 0.5, y > 0.5, \\ (1, 1.206, 1.206, 0.029), & x < 0.5, y < 0.5, \\ (0.5323, 0, 1.206, 0.3), & x > 0.5, y < 0.5. \end{cases} \quad (70)$$

and the computation domain restricted within $[0, 1.0] \times [0, 1.0]$ [38]. All variables are

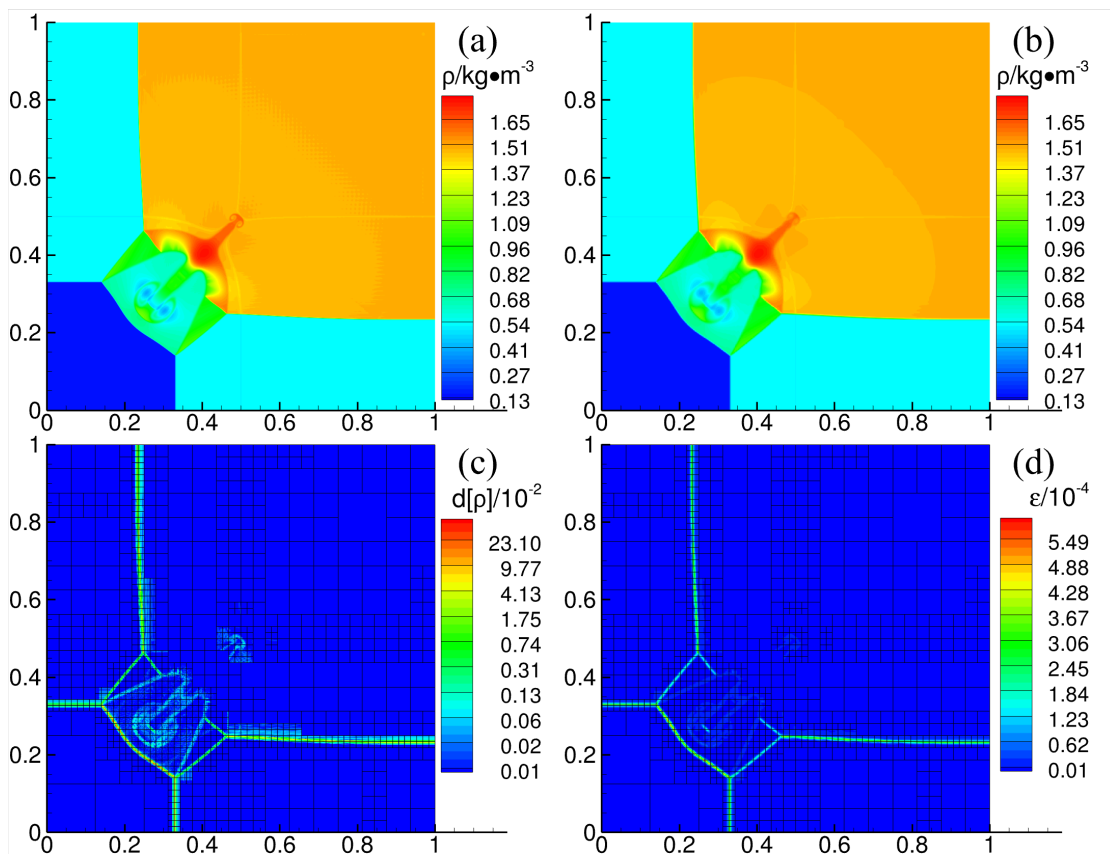


Figure 15: 2D Riemann problem: (a) density contours obtained by 4-order FR scheme on a MR grid with an effective resolution of 512×512 , (b) density contours obtained by 5-order WENO scheme on a MR grid with an effective resolution of 2048×2048 , (c) contours of detail of density with exponentially distributed levels, and (d) distribution of artificial viscosity.

measured in SI units, and the "outflow" condition is applied to each boundary. Our simulation uses the following parameters: $N_{\text{SP}} = 4^2$, $\epsilon = 0.01$, $L_{\text{max}} = 6$, $n_e = 8$, $N_0 = 1$, and $T_{\text{total}} = 0.4\text{s}$. The results of the simulation are presented in Fig. 15. We

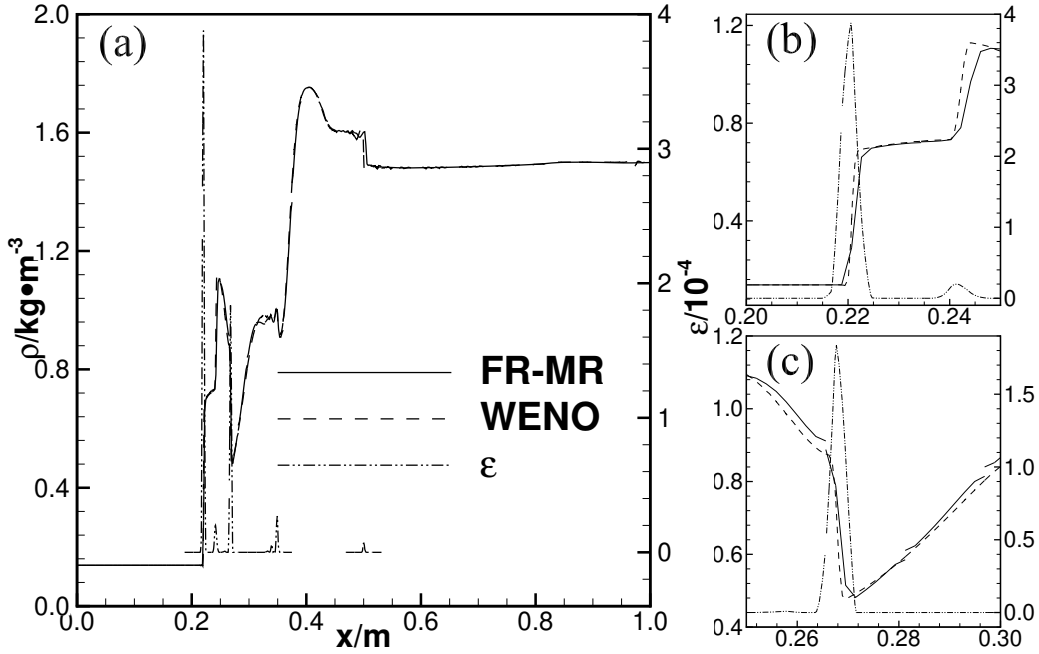


Figure 16: Lines extracted along $y = x$ in the 2D Riemann problem: (a) a global view, (b) an enlarged view of the strongest discontinuity, and (c) an enlarged view of the second strongest discontinuity.

also employ the set for multiresolution grid, i.e., $L_{\max} = 6, n_e = 32$, in FD with a 5-order WENO scheme to obtain a reference solution. As can be seen from Fig. 15(a) and Fig. 15(b), the shocks are accurately captured on the finest grids, and the flow structures simulated by FR-MR and WENO are identical. Observing Fig. 15(c), we can see that the details of density are distributed where shocks appear, which shows that the smoothness indicator perform well. Furthermore, artificial viscosity is added in these regions as shown in Fig. 15(d). Along the diagonal line of the computation domain (specifically, $y = x$), we extract some information to create the plot illustrated in Fig. 16. The density profiles agree well with each other, and the artificial viscosity is applied appropriately in terms of location and magnitude.

5.7. 2D shock-vortex interaction

In order to demonstrate the accuracy of the present method, this subsection simulates 2D shock-vortex interaction [36] within the domain $[0, 2\text{m}] \times [0, 1\text{m}]$. A stationary shock is initially located at $x = 0.5\text{m}$ with a preshock Mach number of $M_s = 1.1$. The left states of the shock are prescribed as

$$(\rho_{L1}, u_{L1}, v_{L1}, p_{L1}) = (1.0 \text{ kg/m}^3, M_s \sqrt{\gamma} \text{ m/s}, 0.0 \text{ m/s}, 1.0 \text{ Pa}), \quad (71)$$

while the right states are determined through the Rankine-Hugoniot jump condition,

$$(\rho_R, u_R, v_R, p_R) \approx (1.169 \text{ kg/m}^3, 1.113 \text{ m/s}, 0.0 \text{ m/s}, 1.245 \text{ Pa}). \quad (72)$$

An isentropic with a center at $(x_c, y_c) = (0.25 \text{ m}, 0.5 \text{ m})$ is prescribed

$$\begin{aligned}
 \rho_{L2} &= \left(1 - \frac{\gamma - 1}{4\alpha\gamma} \varepsilon_2^2 e^{2\alpha(1-\tau^2)} \right)^{1/(\gamma-1)}, \\
 v_\theta &= \varepsilon_2 \tau e^{\alpha(1-\tau^2)}, \quad p_{L2} = \rho_{L2}^\gamma, \\
 u_{L2} &= v_\theta \sin \theta = v_\theta (y - y_c)/r, \\
 v_{L2} &= -v_\theta \cos \theta = -v_\theta (x - x_c)/r, \\
 \tau &= r/r_c, r = \sqrt{(x - x_c)^2 + (y - y_c)^2},
 \end{aligned} \tag{73}$$

with a vortex strength of $\varepsilon_2 = 0.3$, a decay rate of $\alpha = 0.204$, and a critical radius $r_c = 0.05$ at which the vortex reaches its maximum strength. The initial conditions overall are given

$$\begin{cases} (\rho_{L1}\rho_{L2}, u_{L1} + u_{L2}, v_{L1} + v_{L2}, p_{L1}p_{L2}) & \text{if } x < 0.5 \text{ m,} \\ (\rho_R, u_R, v_R, p_R) & \text{if } x \geq 0.5 \text{ m.} \end{cases} \tag{74}$$

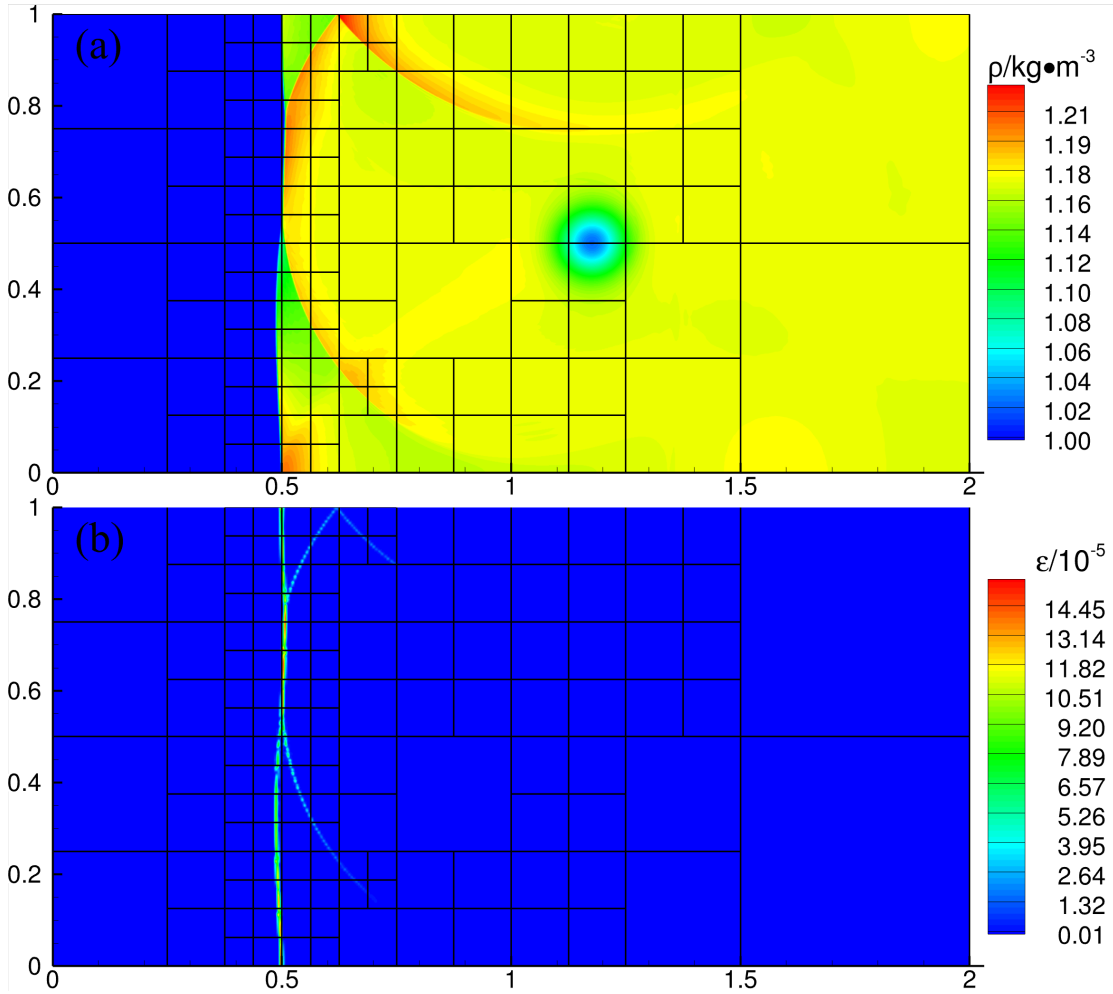


Figure 17: 2D shock-vortex interaction: (a) density contours obtained by 4-order FR scheme on a MR grid with an effective resolution of 768×384 , and (b) distribution of artificial viscosity

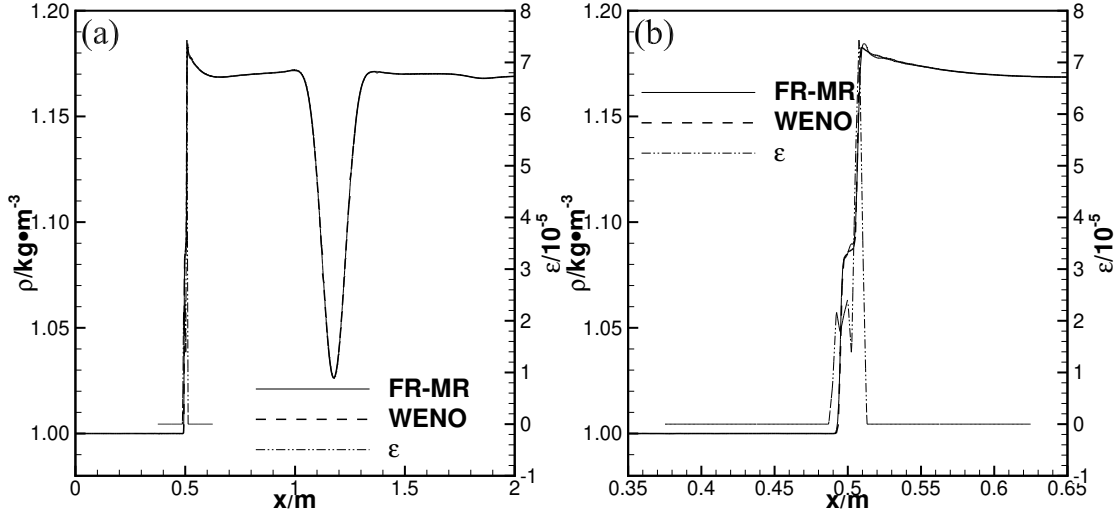


Figure 18: Lines extracted along $y=0.5\text{m}$ in the 2D shock-vortex interaction:(a) a global view, and (b) an enlarged view of the shock

The boundary conditions are specified as follows: (left,right, bottom,top)=(inflow, outflow, slip wall, slip wall). The inflow parameters are prescribed as the left states in Eq. (74). Several important parameters are listed: $N_{\text{SP}} = 4^2$, $\epsilon = 0.01$, $L_{\text{max}} = 4$, $n_e = 24$, $N_0 = 2 \times 1$ (where the two factors correspond to the x and y directions, respectively), and $T_{\text{total}} = 0.8\text{s}$. Contours of density and artificial viscosity at $t = T_{\text{total}}$ are shown in Fig. 17, where it can be observed that the MR algorithm accurately tracks the shock at L_{max} and adds artificial viscosity accordingly. To further validate the simulation, density profiles are extracted along a line at $y = 0.5\text{m}$ and compared with the 5-order WENO result. Fig. 18 demonstrates that the density profiles agree well and the artificial viscosity is effectively incorporated.

5.8. 2D viscous shock tube problem

The purpose of this test case is to establish the accuracy of the present method when the physical viscous terms are significant. For the 2D viscous shock tube, the domain spans $[0, 1.0\text{m}] \times [0, 0.5\text{m}]$ with initial conditions of [39]

$$(\rho, u, v, p) = \begin{cases} (120 \text{ kg/m}^3, 0 \text{ m/s}, 0 \text{ m/s}, 120/\gamma \text{ Pa}), & \text{if } 0 \text{ m} \leq x < 1/2 \text{ m} \\ (1.2 \text{ kg/m}^3, 0 \text{ m/s}, 0 \text{ m/s}, 1.2/\gamma \text{ Pa}), & \text{if } 1/2 \text{ m} \leq x \leq 1 \text{ m} \end{cases} \quad (75)$$

The boundary conditions are as follows: left, right, bottom, top boundaries are prescribed as noslip wall, noslip wall, noslip wall, and symmetry, respectively. The physical viscous terms are prescribed as $Re = 200$ and $Pr = 0.73$, and some parameters are set as follows: $N_{\text{SP}} = 3^2$, $\epsilon = 0.01$, $L_{\text{max}} = 5$, $n_e = 8$, $N_0 = 2 \times 1$, $T_{\text{total}} = 1.0\text{s}$. The simulation results are presented in Fig. 19, which shows the density contours at two separate moments: $t=0.16\text{s}$ (before the right-moving shock has reached the right wall) and $t=1.0\text{s}$ (after the shock has reflected off the right wall). The results obtained using high order FD method (5-order WENO scheme for advection terms and 4-order central difference scheme for diffusion terms) on a 512×256 -cell uniform grid are provided for comparison. As shown in Fig. 19, the grid is refined not only in the vicinity of the shock but also in the boundary layer to capture the fine flow structures. Additionally, we extract some lines from the contours

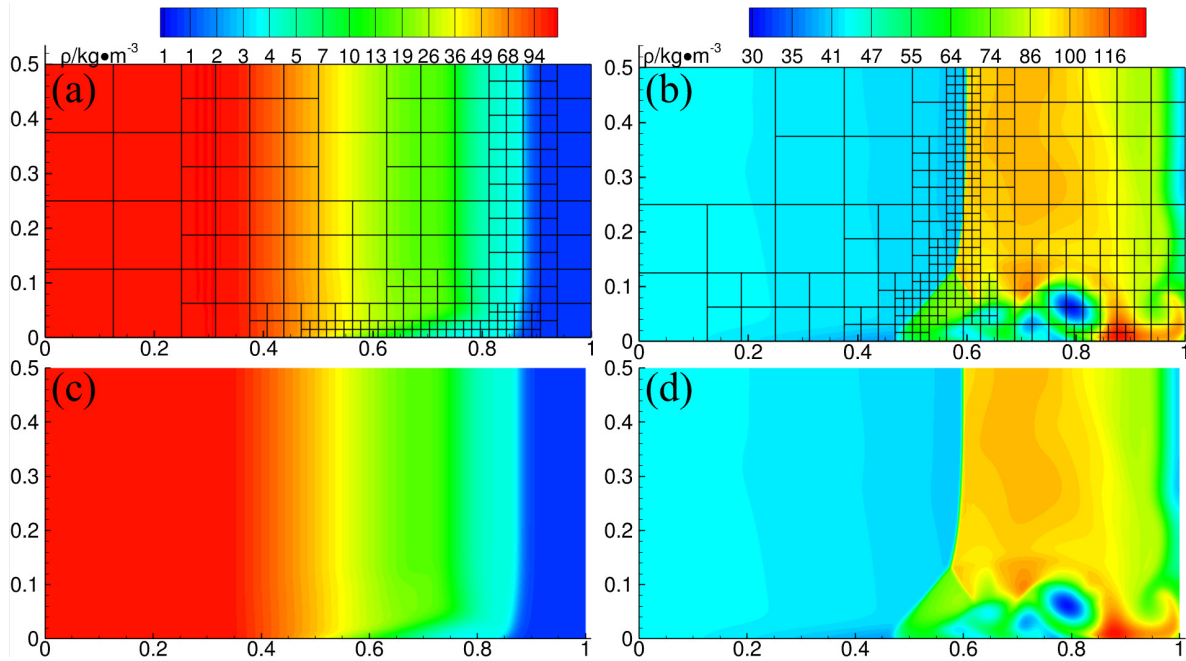


Figure 19: Density contours for 2D viscous shock tube with exponentially distributed levels: the top two subfigures are obtained by 3-order FR scheme on a MR grid with an effective resolution of 512×256 , and the bottom two subfigures are obtained by a 5-order WENO scheme for advection terms and a 4-order central difference scheme for diffusion terms on a uniform grid with 512×256 cells. The two left subfigures are captured at $t = 0.16s$, while the two right subfigures are taken at $t = 1.0s$.

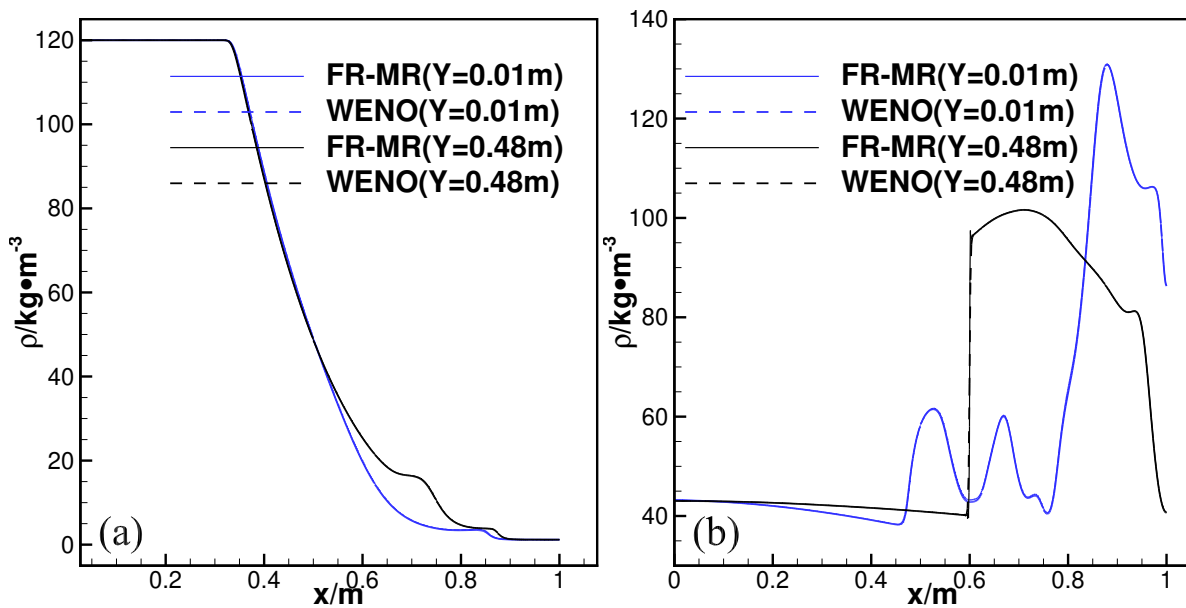


Figure 20: Lines extracted along $y=0.01m$ and $y=0.48m$ in 2D viscous shock tube: (a) $t = 0.16s$, and (b) $t = 1.0s$

and plot them in Fig. 20 for further comparison. The lines extracted at $y = 0.48\text{m}$ demonstrate that the shock is accurately captured, while the lines extracted at $y = 0.01\text{m}$ indicate that the boundary layer is also accurately simulated. This confirms the validity of the viscous terms.

5.9. Double mach reflection

To evaluate the performance of the present method in the presence of a strong shock, a particular test case is chosen for analysis. The prescribed initial conditions for the double Mach reflection problem are [9]

$$(\rho, u, v, p) = \begin{cases} (1.4 \text{ kg/m}^3, 0 \text{ m/s}, 0 \text{ m/s}, 1 \text{ Pa}), & \text{after shock} \\ (8 \text{ kg/m}^3, 7.145 \text{ m/s}, -4.125 \text{ m/s}, 116.8333 \text{ Pa}), & \text{else} \end{cases} \quad (76)$$

and the computation domain is $[0, 4.0\text{m}] \times [0, 1.0\text{m}]$. The strong shock with $\text{Ma}=10$ is initially located along $y = \sqrt{3}(x - 1/6)$. Inflow and outflow conditions are prescribed at the left and right boundaries, respectively. Additionally, the bottom boundary is

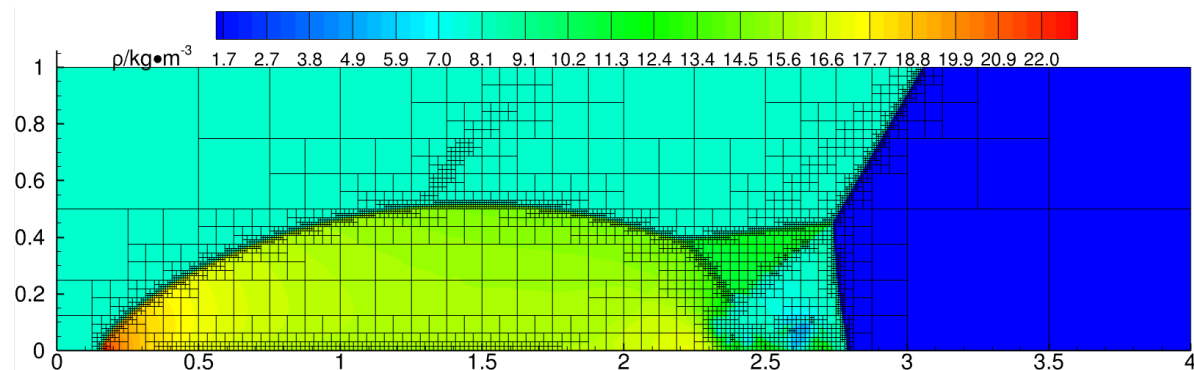


Figure 21: Double mach reflection: density contours obtained by 3-order FR scheme on a MR grid with an effective resolution of 6144×1536 and $L_{\max} = 7$

Table 1: Comparison of the number of blocks ($n_e \times n_e$ elements in each block) between adaptive grids and uniform grids with the effective resolutions at $t = 0.2\text{s}$

L_{\max}	adaptive grids	uniform grids	ratio of blocks
4	346	1024	33.8%
5	784	4096	19.1%
6	1681	16384	10.3%
7	3610	65536	5.5%

assigned inflow for $[0, 1/6\text{m}]$ and slip wall for $[1/6\text{m}, 4.0\text{m}]$, while the top boundary is time-dependently prescribed to track the motion of the strong shock. The inflow parameters are just the post shock states in Eq.(76). Some parameters are listed: $N_{\text{SP}} = 3^2$, $\epsilon = 0.01$, $L_{\max} = 4, 5, 6, 7$, $n_e = 12$, $N_0 = 4 \times 1$, $T_{\text{total}} = 0.2\text{s}$. The simulation results for $L_{\max} = 6$ are displayed in Fig. 21, where the well-resolved flow structures are in good agreement with those simulated by the MR finite difference method [9]. As we can see,

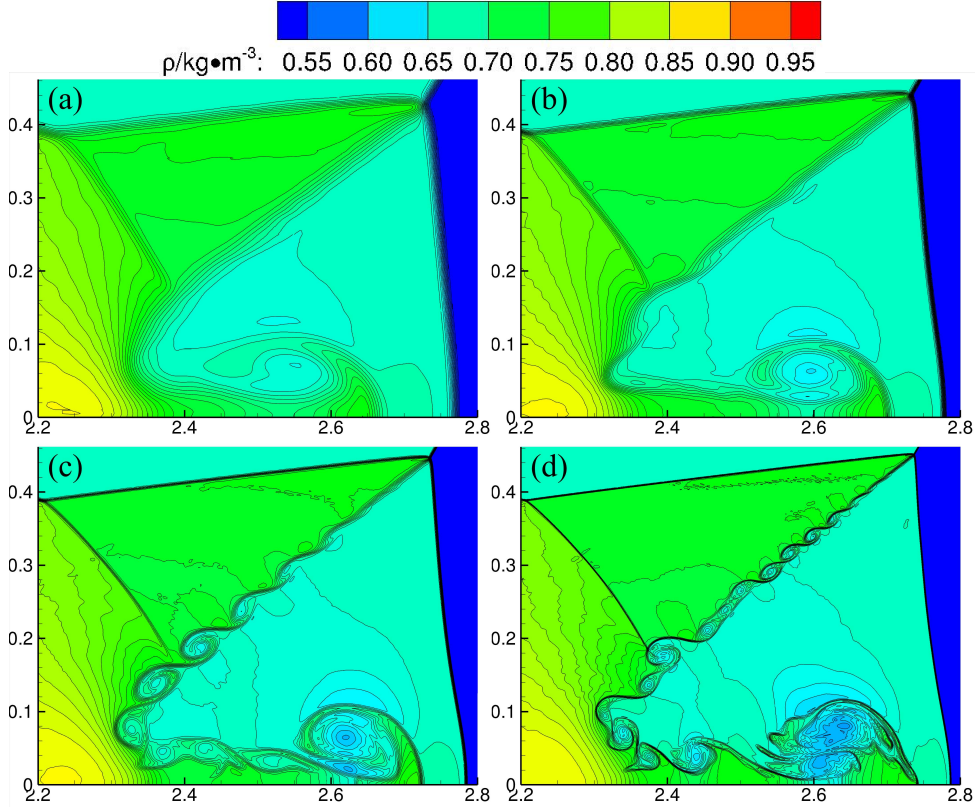


Figure 22: Comparison of fine structures on grids with different resolutions: (a) $L_{\max} = 4$, (b) $L_{\max} = 5$, (c) $L_{\max} = 6$, and (d) $L_{\max} = 7$

the strong shock is well captured by the finest grids while small vortical structures are mainly resolved by the second finest grids. For comparison, Fig. 22 highlights the fine structures on grids with varying L_{\max} . Increasing L_{\max} leads to thinner discontinuities and clearer resolution of vortices. Finally, the number of blocks for adaptive grids with different L_{\max} and uniform grids with the effective resolutions at $t = 0.2\text{s}$ is listed in Table 1. We observe that the ratio of blocks decreases reasonably with increasing L_{\max} .

6. Concluding remarks

In order to simulate compressible flows accurately while reducing computational costs, a multiresolution flux reconstruction method has been developed. This approach leverages a multiresolution algorithm to locate discontinuities at the finest meshes, allowing for precise addition of artificial viscosity using a detail-based indicator. Efficiency is further enhanced by adopting local time stepping, coupled with flux modification on non-conforming interfaces to maintain conservation. Euler vortex flow problem demonstrates that the present MR-FR method keeps the convergence order for smooth flows. Tests on the Euler vortex flow problem have demonstrated that the MR-FR method maintains the convergence order for smooth flows. Riemann and shock-vortex interaction problems in 1D and 2D have demonstrated that the detail-based indicator performs well, and shocks are accurately captured. Viscous shock tube and double mach reflection problems display the validation of our algorithm for flows with physical viscosity and strong shocks, respectively. Furthermore, numerical testing has shown that multiresolution grids prove

significantly more efficient than uniform grids. Future work could extend the present method to higher order time marching schemes using continuous explicit Runge-Kutta methods[35], and could also explore the application of the current work on unstructured grids.

Appendix

In this section, we revisit the projections between adjacent levels mentioned in Sec. 3.2 from the perspective of function spaces. To free us from more irksome mathematical symbols in 2D, we will discuss the topic in 1D; nonetheless, the conclusions derived in this section can be readily extended to 2D and 3D.

First, we define a map

$$\xi = s \cdot z^{(k)} + o^{(k)}, \quad k = 1, 2, \quad (\text{A.1})$$

where the coordinates of the parent element and children elements, ξ and $z^{(k)}$, $k = 1, 2$ respectively, are mapped in form of the standard element, i.e., $\xi, z^{(1)}, z^{(2)} \in [-1, 1]$. For the example depicted in Fig.(23), the scale parameter $s = 0.5$, and the offset parameters $o^{(1)} = -0.5, o^{(2)} = 0.5$. The inverse of the corresponding Eq.(A.1) is

$$z^{(k)} = (\xi - o^{(k)})/s, \quad k = 1, 2. \quad (\text{A.2})$$

For the reconstructed polynomial in *modal* representation, we set

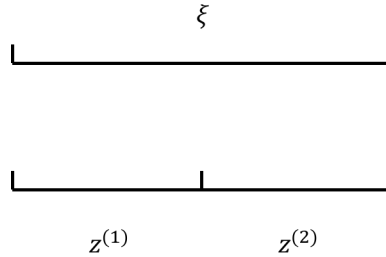


Figure 23: Parent element and children elements in case of 1D

$$q^P(\xi) = \sum_{j=0}^N \tilde{q}_j^P \psi_j(\xi), \quad \xi \in [-1, 1] \quad (\text{A.3})$$

for the parent element, and

$$q^{Ck}(z^{(k)}) = \sum_{j=0}^N \tilde{q}_j^{Ck} \psi_j(z^{(k)}), \quad z^{(k)} \in [-1, 1], \quad k = 1, 2, \quad (\text{A.4})$$

for the children elements, where \tilde{q}_j^P and \tilde{q}_j^{Ck} , $j = 0 \dots N$ denote modal values, and ψ_j , $j = 0 \dots N$ are the basis functions defined in $[-1, 1]$, such as Legendre polynomials. Employing Eq. (A.1) in Eq. (A.3), we obtain

$$\check{q}^{Pk}(z^{(k)}) \stackrel{def}{=} q^P(s \cdot z^{(k)} + o^{(k)}) = \sum_{j=0}^N \tilde{q}_j^P \psi_j(s \cdot z^{(k)} + o^{(k)}), \quad (\text{A.5})$$

$$z^{(k)} \in [-1, 1], \quad k = 1, 2,$$

where the superscript k of \check{q}^{Pk} corresponds to the independent variable $z^{(k)}$. Additionally, we define \check{q}^P using piecewise functions,

$$\check{q}^P \stackrel{def}{=} \begin{cases} \check{q}^{P1}(z^{(1)}), & z^{(1)} \in [-1, 1] \\ \check{q}^{P2}(z^{(2)}), & z^{(2)} \in [-1, 1] \end{cases}. \quad (\text{A.6})$$

Substituting Eq. (A.2) into Eq. (A.4), we get

$$\check{q}^{Ck}(\xi) \stackrel{def}{=} q^{Ck} \left(\frac{\xi - o^{(k)}}{s} \right) = \sum_{j=0}^N \check{q}_j^{Ck} \psi_j \left(\frac{\xi - o^{(k)}}{s} \right), \quad (\text{A.7})$$

$$\xi \in [o^{(k)} - s, o^{(k)} + s], \quad k = 1, 2.$$

Similarly to before, we also employ piecewise functions to define

$$\check{q}^C(\xi) \stackrel{def}{=} \begin{cases} \check{q}^{C1}(\xi) = q^{C1} \left(\frac{\xi - o^{(1)}}{s} \right), & \xi \in [o^{(1)} - s, o^{(1)} + s] \\ \check{q}^{C2}(\xi) = q^{C2} \left(\frac{\xi - o^{(2)}}{s} \right), & \xi \in [o^{(2)} - s, o^{(2)} + s] \end{cases}. \quad (\text{A.8})$$

$$\mathbf{M}_{ij} = \int_{-1}^1 \psi_i(z) \psi_j(z) dz, \quad \mathbf{S}_{ij}^{(k)} = \int_{-1}^1 \psi_i(z) \psi_j(s \cdot z + o^{(k)}) dz, \quad k = 1, 2 \quad (\text{A.9})$$

A.1. Scatter: projection from parent to children

The scatter projection matrix \mathbf{P}^{Sk} proposed by Kopera et al. [31], is derived from the principle of unweighted L^2 projection or least squares approximation of a given function [34], i.e.,

$$\int_{-1}^1 (q^{Ck}(z^{(k)}) - \check{q}^{Pk}(z^{(k)})) \psi_i(z^{(k)}) dz^{(k)} = 0, \quad (\text{A.10})$$

$$i = 0, \dots, N, \quad k = 1, 2,$$

where the known condition, $\check{q}^{Pk}(z^{(k)})$, takes the form of Eq. (A.5). Consider a $(N + 1)$ -dimensional linear space

$$\mathcal{P}_N[-1, 1] = \left\{ p|_{[-1, 1]}; p \in \mathcal{P}_N \right\}, \quad (\text{A.11})$$

where \mathcal{P}_N represents the space of all polynomials with degrees not greater than N . The inner product defined on this space is defined as

$$(f, g) \stackrel{def}{=} \int_{-1}^1 f(t)g(t)dt. \quad (\text{A.12})$$

Dropping the independent variable, $z^{(k)}$ for ease of notation, Eq. (A.10) can be rewritten as

$$(q^{Ck} - \check{q}^{Pk}, \psi_i) = 0, \quad i = 0, \dots, N, \quad (\text{A.13})$$

implying that

$$(q^{Ck} - \check{q}^{Pk}) \perp \text{span}(\psi_1, \psi_2, \dots, \psi_N). \quad (\text{A.14})$$

It is obvious that

$$\text{span}(\psi_1, \psi_2, \dots, \psi_N) = \mathcal{P}_N[-1, 1]. \quad (\text{A.15})$$

Observing Eq. (A.4) and Eq.(A.5), we easily get that

$$q^{Ck}, \check{q}^{Pk} \in \mathcal{P}_N[-1, 1], \quad k = 1, 2, \quad (\text{A.16})$$

and furthermore,

$$q^{Ck} - \check{q}^{Pk} \in \mathcal{P}_N[-1, 1], \quad k = 1, 2. \quad (\text{A.17})$$

Only if

$$q^{Ck} - \check{q}^{Pk} = \boldsymbol{\theta}, \quad k = 1, 2 \quad (\text{A.18})$$

can Eq.(A.14) and Eq. (A.16) both be satisfied, where the zero element of $\mathcal{P}_N[-1, 1]$ is

$$\boldsymbol{\theta}(t) = 0, t \in [-1, 1]. \quad (\text{A.19})$$

By substituting Eq. (A.5) and Eq.(A.19) into Eq. (A.18), we get

$$\begin{aligned} q^{C1}(z^{(1)}) &= \check{q}^{P1}(z^{(1)}) = q^P(s \cdot z^{(1)} + o^{(1)}), \forall z^{(1)} \in [-1, 1], \\ q^{C2}(z^{(2)}) &= \check{q}^{P2}(z^{(2)}) = q^P(s \cdot z^{(2)} + o^{(2)}), \forall z^{(2)} \in [-1, 1]. \end{aligned} \quad (\text{A.20})$$

Further by utilizing Eq.(A.1) and Eq.(A.2), and considering Eq.(A.7), we can rewrite Eq.(A.20) as

$$\begin{aligned} \check{q}^{C1}(\xi) &= q^{C1}\left(\frac{\xi - o^{(1)}}{s}\right) = q^P(\xi), \forall \xi \in [o^{(1)} - s, o^{(1)} + s], \\ \check{q}^{C2}(\xi) &= q^{C2}\left(\frac{\xi - o^{(2)}}{s}\right) = q^P(\xi), \forall \xi \in [o^{(2)} - s, o^{(2)} + s], \end{aligned} \quad (\text{A.21})$$

and show that

$$\check{q}^C(\xi) = q^P(\xi), \forall \xi \in [-1, 1], \quad (\text{A.22})$$

based on Eq.(A.8). Since $q^P \in \mathcal{P}_N[-1, 1]$ (as per Eq.(A.3)), Eq.(A.22) implies that

$$\check{q}^C \in \mathcal{P}_N[-1, 1]. \quad (\text{A.23})$$

It is vital to note that the above derivation does not assume specific values for s and $o^{(k)}$. Therefore, Eq. (A.20) and Eq. (A.22) hold true for any reasonable s and $o^{(k)}$. In case that $s = 0.5, o^{(k)} = \pm 0.5$ and $N = 3, q^P(\xi) = \xi^3$, Eq.(A.22) or Eq.(A.21) is plotted in Fig. (24).

From Eq. (A.20) and Eq. (A.22), it can be concluded that the scatter projection can be simplified to an interpolation operation, and this conclusion can be extended to 2D and 3D straightforwardly. The matrix form of the scatter projection has been provided in Sec. 3.3, and the interpolation operation is as follows. Given the nodal values of parent element, $q_j^P, j = 0, \dots, N$, the reconstructed polynomial for q^P in nodal representation is

$$q^P(\xi) = \sum_{n=0}^N q_n^P L_n(\xi). \quad (\text{A.24})$$

The corresponding Lagrange basis function $L_j(\xi)$ is given by

$$L_j(\xi) = \prod_{n=0, n \neq j}^N \frac{\xi - \xi_n}{\xi_j - \xi_n}. \quad (\text{A.25})$$

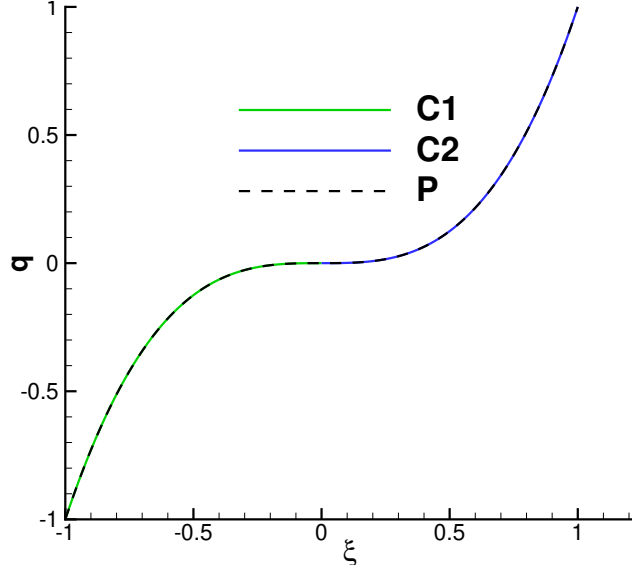


Figure 24: Scatter: $N = 3, q^P(\xi) = \xi^3$

The l -th nodal value of the k -th child element is determined by

$$q_l^{Ck} = q^{Ck}(z_l^{(k)}) = q^P(\xi_l^{(k)}) \quad (\text{A.26})$$

$$\xi_l^{(k)} \stackrel{\text{def}}{=} s \cdot z_l^{(k)} + o^{(k)}.$$

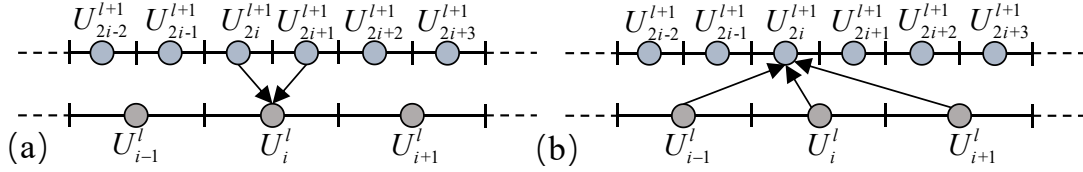


Figure 25: Information communication between two adjacent levels: (a) prediction, and (b) projection [10]

Fig. 25(a) shows the prediction step of MR analysis in the frame of FD, and the corresponding prediction operator is that

$$P_{l \rightarrow l+1} : \begin{cases} \hat{u}_{l+1,2i} = \bar{u}_{l,i} + \sum_{k=1}^m \gamma_k (\bar{u}_{l,i+k} + \bar{u}_{l,i-k}), \\ \hat{u}_{l+1,2i+1} = \bar{u}_{l,i} - \sum_{k=1}^m \gamma_k (\bar{u}_{l,i+k} + \bar{u}_{l,i-k}). \end{cases} \quad (\text{A.27})$$

where $\bar{u}_{l,i}$ is the exact cell-averaged of cell i at level l , and m is the number of required nearest uncles in each direction. The prediction operator is a polynomial interpolation on the cell-average values, and its accuracy is $(2m + 1)$ -th order. The coefficients γ_k for the corresponding interpolation are provided in

$$m = 1 : \gamma_1 = -\frac{1}{8};$$

$$m = 2 : \gamma_1 = -\frac{22}{128}, \quad \gamma_2 = \frac{3}{128}. \quad (\text{A.28})$$

It is clear that with $m = 0$, Eq. (A.27) is equivalent to Eq. (A.24)-(A.26) with $N = 0$.

A.2. Gather: projection from children to parent

Similar to \mathbf{P}^{Sk} discussed in Sec. A.1, the gather projection matrix \mathbf{P}^{Gk} [31] is obtained from

$$\int_{-1}^1 (q^P(\xi) - \check{q}^C(\xi)) \psi_i(\xi) d\xi = 0, \quad i = 0, \dots, N. \quad (\text{A.29})$$

Here the known condition $\check{q}^C(\xi)$, is provided in the form of Eq.(A.8). Let us introduce two infinite-dimensional linear function spaces,

$$\mathcal{C}[-1, 1] = \left\{ f|_{[-1,1]}; f \text{ is continuous} \right\} \quad (\text{A.30})$$

and

$$\mathcal{L}_2[-1, 1] = \left\{ f|_{[-1,1]}; \int_{-1}^1 |f(t)|^2 dt < +\infty, \right\}. \quad (\text{A.31})$$

The inner product defined on both spaces follows the same expression as given in Eq.(A.12). These two spaces satisfy the condition that

$$\mathcal{P}_N[-1, 1] \subsetneq \mathcal{C}[-1, 1] \subsetneq \mathcal{L}_2[-1, 1]. \quad (\text{A.32})$$

Following the procedure outlined in Sec. A.1, we can rewrite Eq.(A.29) as

$$(q^P - \check{q}^C) \perp \text{span}(\psi_0, \dots, \psi_N) = \mathcal{P}_N[-1, 1]. \quad (\text{A.33})$$

This implies that the gather projection error is orthogonal to $\mathcal{P}_N[-1, 1]$. We note that $q^P \in \mathcal{P}_N[-1, 1]$ and $\check{q}^C \in \mathcal{L}_2[-1, 1]$, since \check{q}^C may not be continuous at the joints of two children elements. As demonstrated in Ref. [34], q^P is the least square approximation of \check{q}^C in $\mathcal{P}_N[-1, 1]$. In Fig. 26, we visually depict some examples of this approximation when $s = 0.5$, $o^{(k)} = \pm 0.5$, and $N = 3$.

Based on the derivation presented in Sec. A.1, it can be concluded that

$$q^P(\xi) = \check{q}^C(\xi), \forall \xi \in [-1, 1], \quad (\text{A.34})$$

under the condition that $\check{q}^C \in \mathcal{P}_N[-1, 1]$, which is illustrated in Fig. 26(d). Conversely, if \check{q}^C is not in $\mathcal{P}_N[-1, 1]$, then

$$\exists \xi_0 \in [-1, 1] \quad \text{s.t.} \quad q^P(\xi_0) \neq \check{q}^C(\xi_0), \quad (\text{A.35})$$

which is demonstrated in Fig. 26(a), 26(b), and 26(c).

Fig. 25(b) displays the projection step, which is the counterpart of prediction step shown in Fig. 25(a). The corresponding projection operator is

$$P_{l+1 \rightarrow l} : \bar{u}_{l,i} = \frac{1}{2} (\bar{u}_{l+1,2i} + \bar{u}_{l+1,2i+1}), \quad (\text{A.36})$$

which is identical to gather projection operator in case of $N = 0$.

By rewriting Eq. (A.33) as

$$\int_{-1}^1 (q^P(\xi) - \check{q}^C(\xi)) \psi(\xi) d\xi = 0, \quad \forall \psi(\xi) \in \mathcal{P}_N[-1, 1], \quad (\text{A.37})$$

and specifying $\psi(\xi) = 1, \xi \in [-1, 1]$, we can obtain

$$\int_{-1}^1 q^P(\xi) d\xi = \int_{-1}^1 \tilde{q}^C(\xi) d\xi, \quad (\text{A.38})$$

which is referred to as local conservation in [12]. In the gather projection, some details are lost, i.e.

$$d(\xi) \stackrel{\text{def}}{=} q^P(\xi) - \tilde{q}^C(\xi), \quad (\text{A.39})$$

but the conservation is satisfied. In contrast, the scatter projection retains all information, as illustrated in Eq.(A.20) and Eq.(A.22).

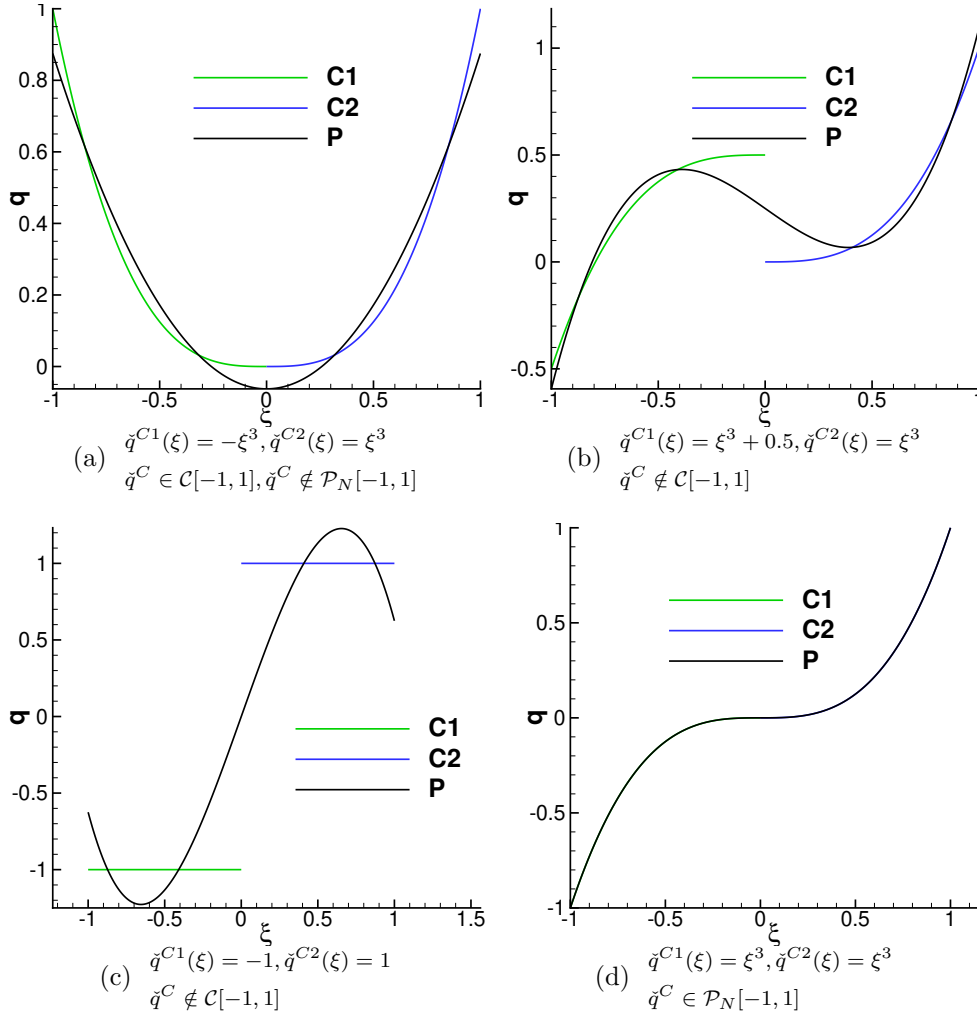


Figure 26: Gather: $N = 3$

A.3. ①Scatter ②Gather: proof of outflow condition

The outflow condition was introduced in Ref. [34] and was subsequently proven for both order and subdomain refinement cases. In our case, this condition can be expressed mathematically as

$$\sum_{k=1}^2 \mathbf{P}^{Gk} \mathbf{P}^{Sk} = \mathbf{I}, \quad (\text{A.40})$$

where \mathbf{I} is the identity matrix. In Ref. [40], Eq. (A.40) was proven, and we provide an alternative proof using the following approach: considering $\forall \bar{q}^P \in \mathcal{P}_N[-1, 1]$, we define

$$\hat{q}^P \stackrel{def}{=} \sum_{k=1}^n \mathbf{P}^{Gk} \mathbf{P}^{Sk} \bar{q}^P, \quad (\text{A.41})$$

so that Eq.(A.40) holds if $\hat{q}^P = \bar{q}^P$. We note that Eq. (A.41) follows the process outlined in Fig. 4(b). With the definition

$$\begin{aligned} \bar{q}^{Ck} &\stackrel{def}{=} \mathbf{P}^{Sk} \bar{q}^P, \quad k = 1, 2, \\ \bar{q}^C &\stackrel{def}{=} \begin{cases} \bar{q}^{C1} \\ \bar{q}^{C2} \end{cases}, \end{aligned} \quad (\text{A.42})$$

Eq.(A.41) can be written as

$$\hat{q}^P = \sum_{k=1}^n \mathbf{P}^{Gk} \bar{q}^{Ck}. \quad (\text{A.43})$$

Based on Eq.(A.22) and Eq.(A.23), we can conclude that

$$\bar{q}^C = \bar{q}^P \quad (\text{A.44})$$

and

$$\bar{q}^C \in \mathcal{P}_N[-1, 1], \quad (\text{A.45})$$

which is a prerequisite for Eq.(A.34). By applying this result, we can deduce that

$$\hat{q}^P = \bar{q}^C. \quad (\text{A.46})$$

Utilizing this information, we can easily prove that in the basis of Eq.(A.44) and (A.46), \hat{q}^P and \bar{q}^P are equal, which satisfies the outflow condition presented in Eq.(A.40). The validity of this proof is evident upon observing Fig. 24 followed by Fig. 26(d).

Additionally, according to Ref [32], the two operators in Eq. (A.27) and Eq. (A.36) are related by

$$P_{l+1 \rightarrow l} \circ P_{l \rightarrow l+1} = \mathbf{I}. \quad (\text{A.47})$$

Significantly, this equivalence is identical to the outflow condition, which is expressed in the form of Eq.(A.40).

A.4. ①Gather ②Scatter: indication of smoothness

In Fig. 4(a), the two operations indicated represent

$$\bar{q}^P \stackrel{def}{=} \sum_{k=1}^2 \mathbf{P}^{Gk} \bar{q}^{Ck} \quad (\text{A.48})$$

and

$$\hat{q}^{Ck} \stackrel{def}{=} \mathbf{P}^{Sk} \bar{q}^P, \quad k = 1, 2, \quad (\text{A.49})$$

respectively. Based on the conclusions drawn by Eq.(A.20) and Eq.(A.35), the errors of the parent element and its children elements stem solely from Eq.(A.48) while Eq.(A.49) yields no error. Further, the smoothness of q can be accurately measured by either the absolute error, $\| \hat{q}^{Ck} - \bar{q}^{Ck} \|$ [17][13], or the relative error, $\| \hat{q}^{Ck} - \bar{q}^{Ck} \| / \| \bar{q}^{Ck} \|$. This is exemplified by the results presented in Fig. 26.

References

- [1] Zhijian J Wang, Krzysztof Fidkowski, Rémi Abgrall, Francesco Bassi, Doru Caraeni, Andrew Cary, Herman Deconinck, Ralf Hartmann, Koen Hillewaert, Hung T Huynh, et al. High-order cfd methods: current status and perspective. *International Journal for Numerical Methods in Fluids*, 72(8):811–845, 2013.
- [2] Hung T Huynh. A flux reconstruction approach to high-order schemes including discontinuous galerkin methods. In *18th AIAA computational fluid dynamics conference*, page 4079, 2007.
- [3] Hung T Huynh. A reconstruction approach to high-order schemes including discontinuous galerkin for diffusion. In *47th AIAA aerospace sciences meeting including the new horizons forum and aerospace exposition*, page 403, 2009.
- [4] Zhi Jian Wang and Haiyang Gao. A unifying lifting collocation penalty formulation including the discontinuous galerkin, spectral volume/difference methods for conservation laws on mixed grids. *Journal of Computational Physics*, 228(21):8161–8186, 2009.
- [5] Peter E Vincent, Patrice Castonguay, and Antony Jameson. A new class of high-order energy stable flux reconstruction schemes. *Journal of Scientific Computing*, 47:50–72, 2011.
- [6] Jingjing Yang, Bin Zhang, Chunlei Liang, and Yongwu Rong. A high-order flux reconstruction method with adaptive mesh refinement and artificial diffusivity on unstructured moving/deforming mesh for shock capturing. *Computers & Fluids*, 139:17–35, 2016.
- [7] Jingjing Yang. *An Adaptive Mesh Refinement High-Order Flux Reconstruction Method for Shock Capturing and Magnetohydrodynamics*. PhD thesis, The George Washington University, 2017.
- [8] Xiaoliang Zhang, Chunlei Liang, and Jingjing Yang. A high-order flux reconstruction/correction procedure via reconstruction method for shock capturing with space-time extension time stepping and adaptive mesh refinement. In *55th AIAA Aerospace Sciences Meeting*, page 0519, 2017.
- [9] LH Han, T Indinger, XY Hu, and Nikolaus A Adams. Wavelet-based adaptive multi-resolution solver on heterogeneous parallel architecture for computational fluid dynamics. *Computer Science-Research and Development*, 26(3):197–203, 2011.
- [10] LH Han, XY Hu, and Nikolaus A Adams. Adaptive multi-resolution method for compressible multi-phase flows with sharp interface model and pyramid data structure. *Journal of Computational Physics*, 262:131–152, 2014.
- [11] Andrew Shelton, Marilyn Smith, and Hao Min Zhou. A multi-resolution discontinuous galerkin method for unsteady compressible flows. In *38th Fluid Dynamics Conference and Exhibit*, page 4140, 2008.

- [12] Nils Gerhard. *An adaptive multiresolution discontinuous Galerkin scheme for conservation laws*. PhD thesis, Universitätsbibliothek der RWTH Aachen, 2017.
- [13] Juntao Huang and Yingda Cheng. An adaptive multiresolution discontinuous galerkin method with artificial viscosity for scalar hyperbolic conservation laws in multidimensions. *SIAM Journal on Scientific Computing*, 42(5):A2943–A2973, 2020.
- [14] Ami Harten. Multiresolution algorithms for the numerical solution of hyperbolic conservation laws. *Communications on Pure and Applied Mathematics*, 48(12):1305–1342, 1995.
- [15] Birgit Gottschlich-Müller and Siegfried Müller. Adaptive finite volume schemes for conservation laws based on local multiresolution techniques. In *Hyperbolic Problems: Theory, Numerics, Applications: Seventh International Conference in Zürich, February 1998 Volume I*, pages 385–394. Springer, 1999.
- [16] Wei Guo and Yingda Cheng. An adaptive multiresolution discontinuous galerkin method for time-dependent transport equations in multidimensions. *SIAM Journal on Scientific Computing*, 39(6):A2962–A2992, 2017.
- [17] Mathea J Vuik and Jennifer K Ryan. Multiwavelet troubled-cell indicator for discontinuity detection of discontinuous galerkin schemes. *Journal of Computational Physics*, 270:138–160, 2014.
- [18] Per-Olof Persson and Jaime Peraire. Sub-cell shock capturing for discontinuous galerkin methods. In *44th AIAA Aerospace Sciences Meeting and Exhibit*, page 112, 2006.
- [19] Guido Lodato. Characteristic modal shock detection for discontinuous finite element methods. *Computers & Fluids*, 179:309–333, 2019.
- [20] Patrice Castonguay, David Williams, Peter Vincent, Manuel Lopez, and Antony Jameson. On the development of a high-order, multi-gpu enabled, compressible viscous flow solver for mixed unstructured grids. In *20th AIAA computational fluid dynamics conference*, page 3229, 2011.
- [21] Francesco Bassi and Stefano Rebay. A high-order accurate discontinuous finite element method for the numerical solution of the compressible navier–stokes equations. *Journal of computational physics*, 131(2):267–279, 1997.
- [22] F Bassi and S Rebay. A high order discontinuous galerkin method for compressible turbulent flows. In *Discontinuous Galerkin Methods*, pages 77–88. Springer, 2000.
- [23] Bernardo Cockburn and Chi-Wang Shu. The local discontinuous galerkin method for time-dependent convection-diffusion systems. *SIAM journal on numerical analysis*, 35(6):2440–2463, 1998.
- [24] Chi-Wang Shu and Stanley Osher. Efficient implementation of essentially non-oscillatory shock-capturing schemes. *Journal of Computational Physics*, 77(2):439–471, 1988.

- [25] Xiangxiong Zhang and Chi-Wang Shu. On positivity-preserving high order discontinuous galerkin schemes for compressible euler equations on rectangular meshes. *Journal of Computational Physics*, 229(23):8918–8934, 2010.
- [26] Xiangxiong Zhang and Chi-Wang Shu. Positivity-preserving high order discontinuous galerkin schemes for compressible euler equations with source terms. *Journal of Computational Physics*, 230(4):1238–1248, 2011.
- [27] Xiangxiong Zhang. On positivity-preserving high order discontinuous galerkin schemes for compressible navier–stokes equations. *Journal of Computational Physics*, 328:301–343, 2017.
- [28] Abhishek Sheshadri. *An analysis of stability of the flux reconstruction formulation with applications to shock capturing*. PhD thesis, Stanford University, 2016.
- [29] Ray Vandenhoeck and Andrea Lani. Implicit high-order flux reconstruction solver for high-speed compressible flows. *Computer Physics Communications*, 242:1–24, 2019.
- [30] Margarete O. Domingues, Sônia M. Gomes, Olivier Roussel, and Schneider Kai. An adaptive multiresolution scheme with local time stepping for evolutionary pdes. *Journal of Computational Physics*, 227(8):3758–3780, 2008.
- [31] Michal A Kopera and Francis X Giraldo. Analysis of adaptive mesh refinement for imex discontinuous galerkin solutions of the compressible euler equations with application to atmospheric simulations. *Journal of Computational Physics*, 275:92–117, 2014.
- [32] Olivier Roussel, Kai Schneider, Alexei Tsigulin, and Henning Bockhorn. A conservative fully adaptive multiresolution algorithm for parabolic pdes. *Journal of Computational Physics*, 188(2):493–523, 2003.
- [33] Cathy Mavriplis. *Nonconforming discretizations and a posteriori error estimators for adaptive spectral element techniques*. PhD thesis, Massachusetts Institute of Technology, 1989.
- [34] David A Kopriva and John H Kalias. A conservative staggered-grid chebyshev multidomain method for compressible flows. *Journal of computational physics*, 125(1):244–261, 1996.
- [35] Brynjulf Owren and Marino Zennaro. Derivation of efficient, continuous, explicit runge–kutta methods. *SIAM journal on scientific and statistical computing*, 13(6):1488–1501, 1992.
- [36] ML Yu, Francis X Giraldo, Melinda Peng, and Zhi-Jian Wang. Localized artificial viscosity stabilization of discontinuous galerkin methods for nonhydrostatic mesoscale atmospheric modeling. *Monthly Weather Review*, 143(12):4823–4845, 2015.
- [37] Jin Seok Park, Meilin Yu, Chongam Kim, and ZJ Wang. Comparative study of shock-capturing methods for high-order cpr: Mlp and artificial viscosity. In *Proceedings of the 8th International Conference on CFD, ICCFD8-2014-0067*, 2014.

- [38] Richard Liska and Burton Wendroff. Comparison of several difference schemes on 1d and 2d test problems for the euler equations. *SIAM Journal on Scientific Computing*, 25(3):995–1017, 2003.
- [39] Virginie Daru and Christian Tenaud. Evaluation of tvd high resolution schemes for unsteady viscous shocked flows. *Computers & fluids*, 30(1):89–113, 2000.
- [40] Bin Zhang and Chunlei Liang. A conservative high-order method utilizing dynamic transfinite mortar elements for flow simulations on curved nonconforming sliding meshes. *Journal of Computational Physics*, 443:110522, 2021.